# **CAMBRIDGE**UNIVERSITY PRESS

#### RESEARCH ARTICLE

# Unveiling mysteries of micro-porous structures in xylem vascular of plants: characterising nutrient transport using electro-hydrodynamics

Jinmay Kalita<sup>1</sup>, Sumit Kumar Mehta<sup>1</sup> and Pranab Kumar Mondal<sup>1,2</sup>

Corresponding author: Pranab Kumar Mondal; Email: mail2pranab@gmail.com

Received: 25 July 2025; Revised: 13 September 2025; Accepted: 3 October 2025

Keywords: electrokinetic microfluidic systems; flow/cell interactions; microscale transport; physiological flows

### Abstract

We unveil the flow and ionic transport characteristics of xylem vessels to establish a correlation between in situ electrical energy generation and plant bioregulation. Scanning electron microscopy of the vascular bundles of Brassica juncea provides detailed features of lumen diameter and the porous pit structures of xylem walls. To investigate the nutrient transport and in situ electrical energy generation, we develop a two-dimensional modelling framework of the xylem vessel that is aligned with the experimental data. The solid wall model of the xylem vessel significantly underestimates axial flow resistance at higher inlet pressures, especially for smaller lumen diameters. Within the considered inlet pressure range, the under-prediction in axial flow resistance ranges from 3.14 \% to 6.78 \% and 0.37% to 1.19% for lumen sizes of 5  $\mu$ m and 15  $\mu$ m, respectively. Our analysis manifests that radial transport of ionic nutrients improves with increased porosity and permeability of the pitted porous wall. In the range of inlet pressure under consideration, it is shown that radial efficiency increases by 793.2 % to 471.9 % when the lumen diameter is reduced from 15  $\mu$ m to 5  $\mu$ m. The increased radial flow efficiency in narrower xylem vessels may support plant survivability under drought stress. Remarkably, we demonstrate that it is not the electrical potential alone, but the combined electrical and hydraulic power that influences plant growth. The amplified hydraulic and electrical power in plants with larger xylem vessels may promote growth attributed to more efficient ionic nutrient transport. We establish that the ratio of specific hydraulic conductivity to electrical conductivity acts as a potential indicator of plant health. This ratio increases with root-side inlet pressure; nevertheless, its dependence on lumen diameter is non-monotonic. The insights gained from the current work may advance the understanding of how in situ electrical stimulation regulates plant bioactivities.

### **Impact Statement**

This research provides novel insights into the electro-hydrodynamically regulated bioactivities of plants, particularly the role of *in situ* electrical energy generation associated with nutrient transport through a xylem vessel. By examining the interplay between xylem vessel geometry, ionic flow and electric potential, we demonstrate how lumen diameter influences axial and radial nutrient flux, and hydraulic and electrical power, which then affect plant health. Our findings show that larger lumen diameters enhance both hydraulic and electrical power, but reduce the electric potential difference, underscoring a complex balance between these factors for optimal plant function. Additionally, the ratio of specific hydraulic to electrical conductivity emerges as a key indicator of plant health, influenced by root-side pressure and vessel size. These insights could shape future agricultural practices, enhancing plant resilience, particularly under stress conditions like drought.

© The Author(s), 2025. Published by Cambridge University Press. This is an Open Access article, distributed under the terms of the Creative Commons Attribution-NoDerivatives licence (https://creativecommons.org/licenses/by-nd/4.0/), which permits re-use, distribution, and reproduction in any medium, provided that no alterations are made and the original article is properly cited.

<sup>&</sup>lt;sup>1</sup>Microfluidics and Phytofluidics Laboratory, Department of Mechanical Engineering, Indian Institute of Technology Guwahati, Guwahati, Assam, India

<sup>&</sup>lt;sup>2</sup>School of Agro and Rural Technology, Indian Institute of Technology Guwahati, Guwahati, India

#### 1. Introduction

Analogous to any commercial electronic devices, plants are integrated with living electrical circuits, essential for their proper functioning and metabolic regulation (de Toledo et al., 2019). Plants are capable of generating electricity due to the intrinsic flow of ionic nutrients along with water through micro-sized xylem vessels. The walls of these vessels are composed of cellulose, which contains carboxylic groups as key components (van Doorn et al., 2011). The carboxylic groups impart a negative zeta potential to the xylem walls (Mason, 1950). Plant membranes exhibit a zeta potential of up to nearly -15 mV (Farquhar & Field, 1971). The flow of ionic nutrient solution over such negatively charged surfaces induces a streaming current due to the downstream accumulation of counter-ions in micro/nanofluidic channels (Vasu & De, 2010; Xie et al., 2024). Hence, the streaming current generated in xylem vessels during pressure-driven flow may facilitate the production of electrical energy within plants. It has been observed that plants exposed to electrical fields exhibit better growth, attributed to various physiobiochemical responses (Scopa et al., 2009). Electrical stimulation at the soil-plant interface favours plant development by promoting transport efficiency, gene expression, enzyme activation and wound healing (Lemström, 1904; Wang & Wang, 2004). Studies have shown that the application of electric fields also increases calcium influx, biosynthesis of secondary metabolites, seed germination and root growth (Graziana et al., 1990; Kaimoyo et al., 2008; Lee & Oh, 2021). Moreover, self-induced biopotential at the plant's rhizosphere region enhances photosynthesis and overall plant development by improving physiological activities such as metabolism, early flowering, fruit size, leaf surface area, node formation and gene expression (Venkata Mohan & Yeruva, 2023). These effects are largely attributed to the increased availability of nutrients, which significantly enhances the concentrations of chlorophyll, proteins and carbohydrates. However, plant growth under electrical stimulation depends critically on the intensity of the electric field and the duration of exposure (Lemström, 1904). Despite these promising findings, quantitative insights into how in situ electrical energy modulates plant bioactivity remains limited. Interestingly, this self-sustained energy generated in xylem vessels could also be harnessed as a renewable energy source (Teng et al., 2018).

Previous studies suggest that the transport of ionic nutrient solutions through xylem vessels is actuated by osmotically generated root pressure and the transpiration pull from leaves (De Boer & Volkov, 2003). At night, the absence of transpiration leads to a reduction in xylem pressure, which in turn decreases the streaming potential (Guha et al., 2024). Xylem vessel morphology plays a crucial role in influencing transport characteristics, with transport efficiency increasing alongside vessel diameter (Qaderi et al., 2019). This flow of nutrient solution interacts with the negatively charged elastic walls of the xylem and the elasticity of the walls is positively correlated with nutrient uptake efficiency (Cosgrove, 1993). Further, xylem walls are equipped with porous pit structures which allow the radial transport of water and nutrients between adjacent vessels (Park et al., 2021). In angiosperms, these pits significantly enhance drought tolerance by improving lateral connectivity (Jansen et al., 2003). Because of the existence of these porous pit structures, the electrical permittivity of xylem vessels is much lesser than that of the flowing ionic nutrient solution (Zimmermann et al., 1995). This contrast in permittivity leads to an ion-partitioning effect, driven by the discontinuity in electrostatic free energy near the solid-liquid interface (Ismayeel et al., 2024). The resulting augmentation in cationic selectivity and pore current under confinement conditions enhances blue energy conversion efficiency (Ismayeel et al., 2024). Thus, the arrangement of porous pits on xylem walls may significantly influence electrical energy generation in plants.

The intricate axio-radial flow of nutrient solution within micro-sized xylem vessels offers significant experimental challenges for accurately characterising the transport mechanisms (Brodersen et al., 2019). Consequently, researchers have increasingly employed computational fluid dynamics (CFD) to investigate local variations in xylem flow fields (Roth, 1996; Xu et al., 2020, 2021). However, studies have found that smooth-walled xylem models underestimate transport efficiency, highlighting the necessity of incorporating pit structures in simulations (Xu et al., 2022). In addition, the xylem vessels with larger diameters encounter higher flow velocities by reducing pressure drop and flow resistance

coefficient (Chen et al., 2015). While these computational models present a preliminary understanding of xylem flow dynamics, none have fully integrated the electrokinetic transport phenomena of ionic nutrient solutions along negatively charged xylem walls.

A comprehensive review of the aforementioned literature reveals the strong influence of electrical stimuli on plant development and the potential of xylem vessels to generate bioelectric signals. Nevertheless, limited work has quantitatively explored how *in situ* electrical energy modulates plant bioactivities resulting from nutrient flow through xylem vessels. In this context, we perform a two-dimensional numerical study to quantify *in situ* electrical energy generation in plants by mimicking realistic flow phenomenon in elastic xylem vessel. To accomplish this, we first conduct a detailed morphological study of xylem vessels to determine key geometric parameters such as lumen diameter and the distribution of wall-bound pit structures These parameters are then used to construct a computational model of the xylem vessel incorporating the pitted porous walls. In the numerical simulations, we investigate the effects of xylem wall porosity, permeability and lumen diameter on transport efficiency, and the generation of electrical and hydraulic energy. We believe this work will open up a new avenue for understanding the relationship between *in situ* electrical energy and physiological responses in plants, potentially guiding future strategies in agriculture.

### 2. Mathematical model and experimental details

### 2.1. Mathematical modelling

We show in Figure 1(a) a typical plant and its anatomical section highlighting different cellular structures along with the axio-radial flow of ionic nutrient solutions through the xylem vessel. The walls of the xylem vessel consist of a porous pit arrangement which enables radial nutrient transport among the adjacent xylem vessels. We schematically show the interface separating the nutrient solution in the lumen and pitted porous xylem wall along with the radial view of the pits in the upper left corner of figure 1(a). Notably, the transport of ionic nutrient solution over the negatively charged xylem walls results in the accumulation of counter-ions in the downstream of the xylem vessel. This phenomenon leads to the development of an electrical double layer and sets in an electric potential difference across the vessel. This electric potential difference triggers the generation of electrical energy in plants. Note that a contrast in electrical permittivity between the nutrient solution and the pitted porous walls of the xylem contributes to the ion-partitioning effect, which significantly affect the energy generation mechanism. It is worth adding here that plants may use this *in situ* electrical energy for their metabolic regulation.

We model the underlying phenomenon through the xylem vessel to estimate the axial and radial nutrient transport in plants. The computational domain mimicking the xylem configuration between a root-side and a shoot-side reservoir (radius and height as 25  $\mu$ m and 27.5  $\mu$ m) is shown in the left side of Figure 1(b). Note that we included reservoirs deliberately in the computational domain essentially to stabilise the numerical simulations. In Figure 1(b), the internal radius of xylem (lumen) is  $r_l$  (= 0.5D) and the pitted porous wall thickness is t. The values of  $r_l$  and t are determined from scanning electron microscopy (SEM). Considering the laminar, incompressible flow of ionic nutrient solution, the governing equations describing the transport of ionic nutrients, flow field and the interfacial electrokinetic interaction can be expressed as follows.

The induced electric field in the xylem vessel is governed by the Poisson equation as follows (Sadeghi et al., 2019; Teodoro et al., 2024):

for lumen: 
$$\nabla \cdot (\varepsilon_{xl} \nabla \psi) = -F \sum_{i=1}^{6} z_i c_i;$$
 (1)

for pitted porous wall: 
$$\nabla \cdot (\varepsilon_{xp} \nabla \psi) = -F \sum_{i=1}^{6} z_i c_i,$$
 (2)

where  $\varepsilon_{xl}$  and  $\varepsilon_{xp}$  are the electrical permittivity of nutrient solution in the lumen and pitted porous wall of the xylem vessel, respectively. The values of the corresponding relative permittivity (equivalently,

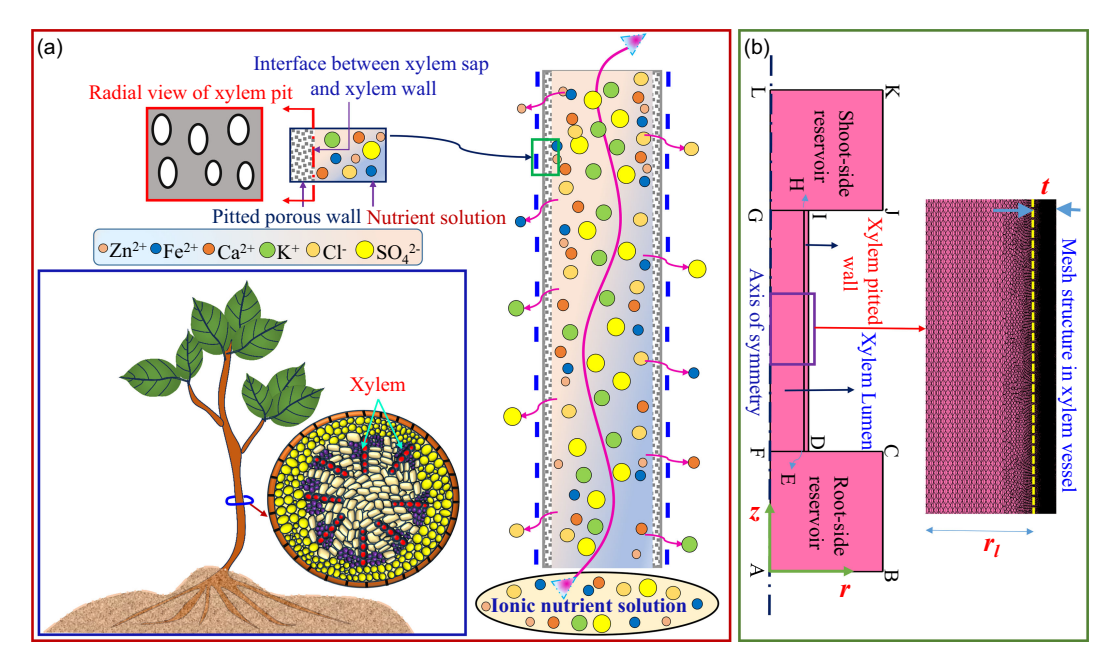


**Figure 1.** (a) A typical plant and its anatomical section showcasing different cellular structures along with an enlarged view of axio-radial transport phenomena of ionic nutrient solution (water +  $K^+$  +  $Ca^{2+}$  +  $Fe^{2+}$  +  $Zn^{2+}$  +  $Cl^-$  +  $SO_4^{2-}$ ) through the xylem vessel having pitted porous wall. (b) Computational domain of the xylem vessel with an enlarged view of mesh structures.

permittivity ratio),  $\varepsilon_{xl}/\varepsilon_0$  and  $\varepsilon_{xp}/\varepsilon_0$  are taken as 78 and 7 (Hu et al., 2025; Zimmermann et al., 1995), respectively. The induced electric potential, Faraday's constant (= 96 485 C mol<sup>-1</sup>), valency of ionic nutrients and concentration of the ionic nutrients are denoted by the symbols  $\psi$ , F,  $z_i$  and  $c_i$ , respectively. Here, i stands for the number of ions available in the nutrient solution which are K<sup>+</sup>, Ca<sup>2+</sup>, Fe<sup>2+</sup>, Zn<sup>2+</sup>, Cl<sup>-</sup> and SO<sub>4</sub><sup>2-</sup> in our study.

Further, the ionic nutrient concentration field inside the xylem vessel can be obtained by solving the Nernst–Planck equation as (Khatibi et al., 2021)

for lumen: 
$$\nabla \cdot \left( -D_{xl,i} \nabla c_i - z_i \frac{D_{xl,i}}{RT} F c_i \nabla \psi \right) + \boldsymbol{u} \cdot \nabla c_i = 0,$$
 (3)

for pitted porous wall: 
$$\nabla \cdot \left( -D_{xp,i} \nabla c_i - z_i \frac{D_{xp,i}}{RT} F c_i \nabla \psi \right) + \boldsymbol{u} \cdot \nabla c_i = 0.$$
 (4)

Here,  $D_{xl,i}$ , and  $D_{xp,i}$  are the diffusion coefficients of ionic nutrients in the lumen and pitted porous walls of the xylem, respectively. The diffusion coefficients inside the xylem lumen  $(D_{xl,i})$  for  $K^+$ ,  $Ca^{2+}$ ,  $Fe^{2+}$ ,  $Zn^{2+}$ ,  $Cl^-$  and  $SO_4^{2-}$  ions are taken as  $1.960 \times 10^{-9}$ ,  $0.793 \times 10^{-9}$ ,  $0.719 \times 10^{-9}$ ,  $0.715 \times 10^{-9}$ ,  $2.030 \times 10^{-9}$  and  $1.070 \times 10^{-9}$  m<sup>2</sup> s<sup>-1</sup>, respectively (Vanýsek, 1972). As the pitted porous wall of the xylem vessel are porous in nature, the diffusion coefficient of ionic nutrients in the xylem lumen  $(D_{xp,i})$  is estimated by employing the Millington and Quirk model as  $D_{xp,i} = \epsilon^{4/3} D_{xl,i}$  (Millington & Quirk, 1961); here,  $\epsilon$  is the pitted porous wall porosity. Moreover, R, T and u represent the universal gas constant (= 8.314 J mol<sup>-1</sup>K<sup>-1</sup>), absolute temperature (= 298 K) and velocity vector, respectively. The r and z components of u are taken as  $u_r$  and  $u_z$ , respectively.

We use the following equations to describe the flow field in the xylem vessel. Continuity equation (Mehta & Mondal, 2024):

$$\nabla \cdot \boldsymbol{u} = 0. \tag{5}$$

Momentum transport equation (Louf et al., 2018; Sadeghi et al., 2019; Teodoro et al., 2024):

for lumen: 
$$\rho(\mathbf{u} \cdot \nabla)\mathbf{u} = -\nabla p + \mu \nabla^2 \mathbf{u} + (F \Sigma z_i c_i)(-\nabla \psi);$$
 (6)

for pitted porous wall: 
$$\frac{\rho}{\epsilon} (\mathbf{u} \cdot \nabla) \frac{\mathbf{u}}{\epsilon} = -\nabla p + \frac{\mu}{\epsilon} \nabla^2 \mathbf{u} - \frac{\mu \mathbf{u}}{k} + (F \Sigma z_i c_i) (-\nabla \psi),$$
 (7)

where  $\rho$ , p and  $\mu$  are the density of the nutrient solution (= 1000 kg m<sup>-3</sup>), the pressure within the xylem vessel and the dynamic viscosity of the ionic nutrient solution. Wen et al. (2023) found that the viscosity of xylem sap is nearly similar to that of pure water. The xylem liquid viscosity is therefore taken to be 0.001 Pa s, as Jensen et al. (2016) also employed in their two-dimensional simulation. The permeability of pitted porous walls is denoted by k. Note that the permeability is calculated by analysing the images captured through SEM of the xylem vessels.

The structural deformation of the xylem walls caused by the internal mechanical stress, resulting from flow loading due to transport of ionic nutrient solution through the porous xylem, is solved considering two-way coupled equations as described below. The governing equation for the deformation field can be described as follows (Panja et al., 2024):

$$\nabla (\mathbf{F} \, \mathbf{S})^T = 0. \tag{8}$$

Here, F and S are the displacement gradient and second-Piola–Kirchhoff stress, respectively; and F is associated with the displacement field  $(V_S)$  as follows:

$$F = I + \nabla V_S, \tag{9}$$

where I is the identity matrix and S can be expressed as

$$S = 2\mu_L \bar{\varepsilon} + \lambda_L tr(\bar{\varepsilon})I. \tag{10}$$

Here,  $\bar{\varepsilon}$  denotes the Lagrange–Green strain and is defined as  $\bar{\varepsilon} = 0.5(F(F)^T - I)$ . The first and second Lamé parameters, which are used in (10), are expressed as follows (Panja et al., 2024):

$$\lambda_L = \nu E/(1+\nu)(2\nu-1), \quad \mu_L = E/2(1+\nu),$$
 (11)

where E (= 500 MPa) (Park et al., 2021) and  $\nu$  (= 0.3) (Karam, 2005) are Young's modulus and Poisson's ratio of the xylem, respectively. We can estimate the Cauchy stress tensor by the following correlation:

$$\overline{\sigma} = \frac{1}{I} (FS(F)^T). \tag{12}$$

In (12), J denotes the Jacobian of F.

We solve the above-mentioned equations by employing physically consistent boundary conditions in the computational domain. We show the boundary conditions used to solve each equation separately through the schematic depiction in Figure 2. For the potential field ((1) and (2)), at the top and bottom reservoir wall,  $\partial \psi/\partial z = 0$ , for the side wall of the reservoir,  $\psi = 0$ ; and for the centreline,  $\partial \psi/\partial r = 0$ . Due to the reservoir potential's non-physical contribution to the xylem vessel, these neutral boundary conditions for the reservoir boundaries are chosen. Here, the reservoir is solely used to numerically solve the ionic transport field for the xylem vessel. It is obvious that there is no reservoir in the actual xylem vessel and the reservoir condition is set solely for numerical purposes. Furthermore, the potential of the xylem wall is set at  $\psi = -15$  mV. For (3) and (4), the bottom side of the reservoir is set as  $c_i = C_{\text{root-side},i}$ and top wall concertation of nutrient is set based on the concentration gradient  $(\partial c_i/\partial z)$  available in the xylem vessel (discussed in the upcoming section) as  $c_i = c_{\text{root-side},i} + (\partial c_i/\partial z)l$  (Khan et al., 2020). The reservoir side boundaries and vessel wall are set as  $\mathbf{n} \cdot (-D_{xp,i} \nabla c_i - z_i \frac{D_{xp,i}}{RT} F c_i \nabla \psi) = 0$ , which is zero-diffusive and migration flux; and the central line is set as  $\frac{\partial c_i}{\partial r} = 0$  because of the symmetry nature of the domain. It is noted that the dominant convective radial ionic flow (ionic Péclét number >> 1) at the xylem pitted porous wall allows non-zero ionic nutrient flow. Moreover, at the interface between the pitted porous wall and free bulk electrolyte, the ion-partitioning effect is taken to consider the Born energy difference generated by the electrical permittivity difference as  $f_{ip} = \exp(-\Delta w_i/k_B T)$ ,

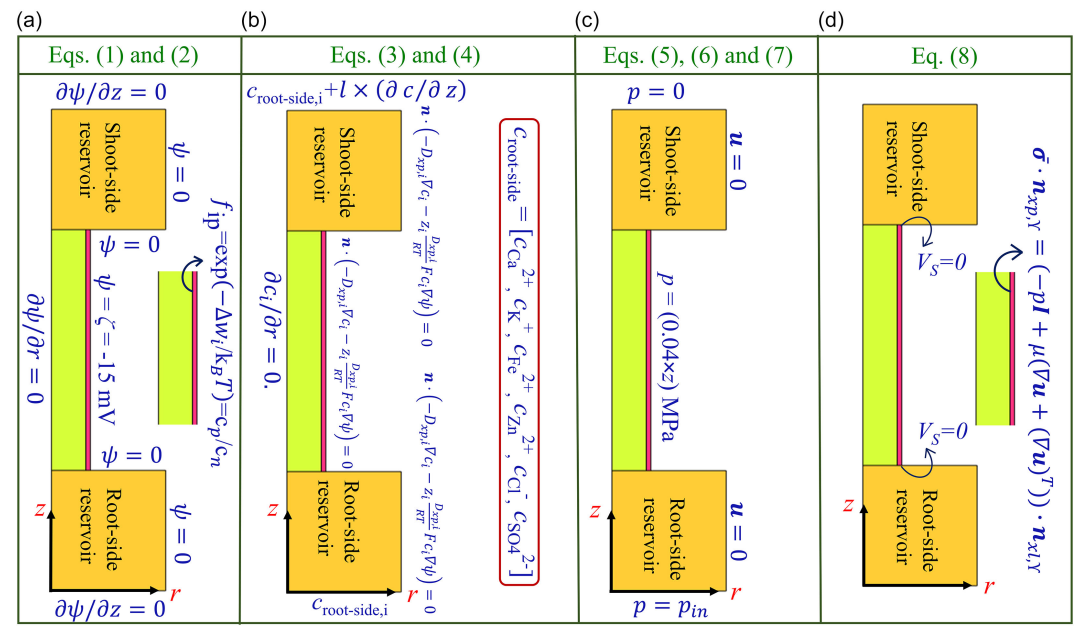


**Figure 2.** Representation of boundary conditions employed in the computational domain to solve the transport equations governing nutrient flow through the xylem vessels: (a) for obtaining the induced electric field [(1)-(2)]; (b) ionic species concentration field [(3)-(4)]; (c) flow field [(5)-(7)] and (d) deformation field [(8)].

and details are presented in the upcoming paragraph. To solve (5)–(7), the top reservoir pressure is set as p=0 and the bottom part (shoot-side) pressure is imposed as  $p=p_{in}$ . Here,  $p_{in}$  is set based on the pressure gradient available in the xylem vessel which actually drives the flow. The previous experimental evidence underscores that the xylem pressure gradient ranges from 0.1 to 20 MPa m<sup>-1</sup> among various plant species (Hellkvist et al. 1974). Thus, following this reported data, we consider the range of root-side pressure  $(p_{in})$  and a constant shoot-side pressure as 10 to 50 Pa and 0 Pa, respectively, for the xylem length of 55  $\mu$ m for the mentioned range of pressure gradient. Moreover, the pressure at the xylem outer wall is set based on the apoplast pressure according to the pressure gradient of that region as  $p=(0.04\times z)$  MPa (Cabrita et al., 2013). For (8), the fixed boundary  $(V_S=0)$  is taken at the ends of the pitted porous wall. The structural interaction of the pitted porous wall with bulk flow is coupled as  $\overline{\sigma}\cdot n_{xp,\Upsilon} = (-pI + \mu(\nabla u + (\nabla u)^T))\cdot n_{xl,\Upsilon}$ . Here,  $n_{xp,\Upsilon}$  and  $n_{xl,\Upsilon}$  are the outward normal in the pitted porous domain and free liquid domain at the interface, respectively.

We consider the ion-partitioning effect, which takes into account the free energy difference caused by the differential in electrical permittivity between the free ionic nutrient solution and the pitted porous walls of the xylem vessel. We introduce an ion-partitioning factor  $(f_{ip})$  to precisely anticipate the ionic distribution close to the interface. The ion-partitioning factor can be defined as the concentration ratio of mobile ionic concentration within the pitted porous wall of the xylem vessel  $(c_p)$  to the ionic nutrients at the free region  $(c_n)$  (Khatibi et al., 2021) close to the interface. Thus, we employ the boundary condition for Nernst-Planck's equation at the interface as  $f_{ip} = \exp(-\Delta w_i/k_B T) = c_p/c_n$ , where  $\Delta w_i = [(ez_i)^2/8\pi r_i]\{(1/\varepsilon_{xp}) - (1/\varepsilon_{xl})\}$  is the Born energy difference and  $r_i$  is the radius of hydrated ionic nutrient species, i (Khatibi et al., 2021). The values of  $r_i$  are taken as 3.31, 4.12, 4.30, 2.15, 3.32, 3.79 Å for K<sup>+</sup>, Ca<sup>2+</sup>, Fe<sup>2+</sup>, Zn<sup>2+</sup>, Cl<sup>-</sup> and SO<sub>4</sub><sup>2-</sup>, respectively (Kielland, 1937; Paul et al., 2012). The ionic concentration of different ionic species in the root-side reservoir is taken as follows:  $c_{K^+} = 0.0256$  mol m<sup>-3</sup>,  $c_{Ca^{2+}} = 0.0625$  mol m<sup>-3</sup>,  $c_{Ca^{$ 

reported inference, the concentration of different ionic species is implemented close to the shoot-side reservoir and given as  $c_{\rm K^+} = 0.0256 + (-1.1076 \times 10^{-6}) \times l$  mol m<sup>-3</sup>,  $c_{\rm Ca^{2+}} = 0.0625 + (7.5 \times 10^{-2}) \times l$  mol m<sup>-3</sup>,  $c_{\rm Fe^{2+}} = 0.06858 + (3.58 \times 10^{-2}) \times l$  mol m<sup>-3</sup>,  $c_{\rm Zn^{2+}} = 0.06057$  mol m<sup>-3</sup>,  $c_{\rm Cl^-} = 0.01$  mol m<sup>-3</sup> and  $c_{\rm SO_4^{-2-}} = 0.1$  mol m<sup>-3</sup>. Here, l is the length of the xylem vessel, which is 55  $\mu$ m in our study.

The radial transport of ionic nutrients among the adjacent xylem vessels is essential for the survival of plants subjected to drought-induced stresses (Jansen et al., 2003). Hence, we undertake an effort to calculate the radial flow of ionic nutrients associated with the radial transport  $(q_r)$  through the pitted porous wall of a xylem vessel using the following mathematical expression:

$$q_r = \frac{\int_{r=r_l}^{r=r_l+t} u_r c_i \, dr}{\int_{r=r_l}^{r=r_l+t} dr}.$$
 (13)

Here,  $u_r$  and  $c_i$  are the radial flow velocity and concentration of the *i*th nutrients and dr is the radial element in the pitted porous wall. The radial nutrient flow is calculated as the averaged convective nutrient flux in (13). Using the flow velocity order of  $\sim 10^{-2}$  m s<sup>-1</sup>, the nutrient ionic diffusion coefficient order of  $\sim 10^{-9}$  m<sup>2</sup> s<sup>-1</sup> (Vanýsek, 1972) and the xylem lumen dimeter order of  $\sim 10^{-5}$  m, the order of the ionic Péclét number is derived as  $\sim 10^2$ . As a result, the convection strength of ionic transport dominates diffusion-based transport. Therefore, to estimate the radial nutrient flow, we have used the convective flux  $(u_r c_i)$ .

Further, to estimate the effect of the pitted porous wall of the xylem vessel on the radial transport of ionic nutrients, we estimate the corresponding radial efficiency as expressed as (Xu et al., 2020)

$$\eta_r = \frac{F_1 - F_2}{F_1} = \frac{Q_2 - Q_1}{Q_2}.\tag{14}$$

Here,  $F_1$  and  $F_2$  are the resistance to the underlying radial flow in the xylem vessel with porous structures and without porous structures on the walls. The radial net flow is represented by the term  $(Q_2 - Q_1)$ . The flow resistance in both cases is calculated as  $F_m = \frac{\Delta p_m}{Q_m}$ ; where  $\Delta p_m$  and  $Q_m = \frac{\pi}{4}D^2u_{zAvg,m}$  are the pressure drop inside the xylem vessel and the corresponding flow rate, respectively. The average axial velocity is denoted by  $u_{zAvg,m}$ , where m = 1, 2 stands for xylem vessels having porous structures and without porous structures on the walls, respectively.

After computing the flow field, ionic concentration distribution and potential field, we numerically estimate the magnitude of the axial *in situ* electric field  $(E_s)$  as an axial gradient of the potential field. Moreover, we determine the electric potential difference  $(V_S)$  that develops due to ionic transport through the xylem vessel by using the expression of  $V_S = E_S l$ . Now, to calculate *in situ* electrical power in plants, we estimate the net axial ionic current  $(I_z)$  in the xylem vessels as (Jafari et al., 2024; Khatibi et al., 2021)

$$I_z = \int_{r=0}^{r=r_l} F\left(-D_{xp,i}\nabla c_i - z_i \frac{D_{xp,i}}{RT} F c_i \nabla \psi\right) dA \int_{r=0}^{r=r_l} dA.$$
 (15)

Here, the limit of the integral is from r = 0 to  $r = r_l$  and elemental cross-sectional area,  $dA = 2\pi r dr$ . This leads us to determine the electrical power generated in the plants as

$$P_{electric} = V_s I_z. (16)$$

Also, the hydraulic power available in the xylem vessels due to the flow of ionic nutrient solution can be estimated by the expression  $Q\Delta p$  (Sarkar, 2020). Again, to examine the flow efficiency of xylem vessels, we define hydraulic conductivity (K) which can be expressed as (Melcher et al., 2012; Quintana-Pulido et al., 2018)

$$K = \frac{\rho Q l}{\Lambda p A}.\tag{17}$$

Here, A is the cross-sectional area of lumen and is expressed as  $A = 0.25\pi D^2$ .

We estimate the electrical conductivity of the ionic nutrient solution present in the xylem vessel to assess the ability of the ionic nutrient solution to transmit electricity in plants. The mathematical

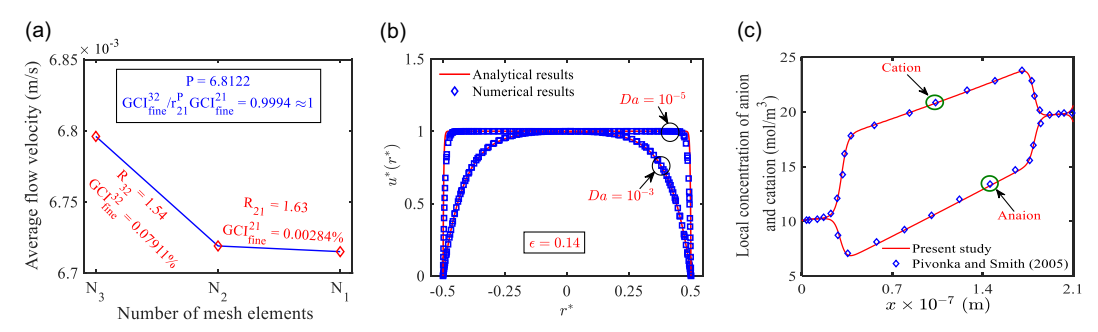


**Figure 3.** (a) Plot showing the average axial flow velocity at the mid cross-section of the xylem vessel for different mesh elements obtained using grid convergence index. Benchmarking of the present numerical model with (b) analytically obtained non-dimensionalized axial velocity profile at a given cross-section of a partially porous microcylinder having  $\epsilon = 0.14$  and Darcy number (Da) =  $10^{-5}$  and  $10^{-3}$ , and (c) with the results of Pivonka & Smith (2005) for local cationic and anionic concentration along the axial centreline of a nanofluidic channel having height = 10 nm and surface charge density =  $-0.01 \text{ C m}^{-2}$ .

expression for electrical conductivity can be outlined as (Heaney, 2004)

$$\sigma = \frac{I_z l}{V_s A}.\tag{18}$$

# 2.2. Numerical methodology and model benchmarking

Considering a two-dimensional configuration, we numerically solve the governing equations, describing electrokinetically modulated transport through the xylem vessel by employing the boundary conditions stated in the preceding subsection. We use the finite element framework of COMSOL Multiphysics to solve how the induced potential develops due to electrical double layer effect, flow field, ionic concentration distribution in the domain and displacement fields. We split the computational domain into smaller non-uniform triangular shaped elements, as shown in the right side of figure 1(b). We use the linear shape function for flow velocity and pressure, quadratic serendipity shape function for displacement, and quadratic shape function for both the ionic concentration and electric potential fields to produce the global matrix system. Each governing equation is separately solved using a segregated solver in such a way that the flow and displacement fields are solved using the parallel direct sparse solver (PARDISO), while the concentration and electric fields are solved by adopting the multifrontal massively parallel sparse direct solver (MUMPS). Subsequently, we have conducted a grid independence test with 29 359, 69 252 and 184 216 meshing elements. In this context, we appeal to the Richardson extrapolation method-based grid convergence index (GCI) (Celik et al., 2008) to calculate the error of the numerical scheme employed in this study. We undertake this endeavour to ascertain that our numerical results become independent of the number of mesh elements considered. To this end, we estimate the average axial flow velocity at the mid-cross-sectional line of the xylem vessel as a key variable of this method. The details of the mathematical calculations of GCI are presented in Appendix A. The results of our analysis are consistent with two different grid convergence indices,  $GCI_{fine}^{21} = 0.00284\%$  and  $GCI_{fine}^{32} = 0.07911\%$ , which allow us to obtain an asymptotic solution satisfying the criterion  $GCI_{fine}^{32}/R_{21}^PGCI_{fine}^{21}=0.9994\approx 1$ , as depicted in Figure 3(a). Following this analysis, we perform simulations for all the cases considered in the current study with  $N_2$  (= 69 252) mesh elements to minimise the involved computational cost without compromising the accuracy of the numerical

Further, we undertake an effort to benchmark our numerical model from two different perspectives. To this end, we compare our simulated results with the analytically obtained dimensionless velocity profile (cf. Appendix B) in a partially porous microcylinder, as depicted in Figure 3(b). We observe a fairly

accurate match between our numerical results and the analytical velocity profile for two different values of Darcy number (Da) equal to  $10^{-5}$  and  $10^{-3}$ . In the second effort, we obtain the ionic concentration field from the present model and compare our results with the reported data of Pivonka & Smith (2005).

Note that the electrokinetic movement of cations and anions of NaCl solution through a nanochannel having height and surface charge density equal to 10 nm and  $-0.01 \,\mathrm{C\,m^{-2}}$ , respectively, is considered to plot the variations depicted in Figure 3(c). For this part, the bulk ionic concentrations of left-side and right-side reservoirs are maintained as 20 mol m<sup>-3</sup> and 10 mol m<sup>-3</sup>, respectively. The promising agreement between the current and the reported results confirms the accuracy of our numerical model developed in this endeavour.

# 2.3. Experimentation: estimation of xylem vessel diameter, porosity and permeability of pitted porous wall

We experimentally measure the diameter of the xylem vessels, the porosity and the permeability of the pitted porous wall. This information is very much needed for numerical simulations towards estimating nutrient flux through the xylem vessels. For this part, we conduct SEM of the anatomical sections of the root and stem of a thirty days old plant of *Brassica juncea*, grown in the green house of the Translational Crop Research Laboratory, Indian Institute of Technology, Guwahati, during the month of October, 2024. The seeds were procured from the Indian Agricultural Research Institute (IARI) Regional Station, Karnal, Haryana, India. The obtained seeds were surface sterilised with 4 % sodium hypochlorite solution (w/v) to avoid any pathogenic contamination. Subsequently, the seeds were repeatedly rinsed three times with autoclaved double-distilled water to eliminate any chemical residue. After the rinsing operation, the seeds were sown in pots containing one and half kg of soil each. During the growth period, necessary water was supplied to the plants upholding standard agricultural practices. The average temperature and relative humidity of the atmosphere were  $33 \pm 2^{\circ}$ C and  $78 \pm 5\%$ , respectively, throughout the growth period of the plants.

To perform SEM, a root and a stem segment of 2 cm length were collected from a healthy plant on the  $30^{th}$  day after sowing the seeds in the soil. Subsequently, thin lateral and longitudinal sections were extracted from the root and stem segments and preserved in 2.5 % glutardialdehyde prepared in 0.1 M sodium phosphate buffer for 2 hr at 4 °C, maintaining the previously established protocol by Nikara et al. (2020). The plant samples were then sequentially dehydrated with 25 %, 50 %, 70 %, 90 % and 100 % of ethanol for 15 min each. The samples were further dried using hexamethyldisilazane (HDMS) overnight to prepare them for imaging. The images were captured by a field emission scanning electron microscope (Zeiss®, Sigma 300). In Figure 4(a), we represent the images of multiple xylem vessels along with an enlarged view of a xylem vessel with pitted porous wall. The xylem lumens observed in SEM images are nearly cylindrical in shape having circular cross-sections. Further, we show the zoomed in view of xylem wall pits of both root and shoot sides of the plant in Figures 4(b) and 4(c), respectively. The shape of the xylem pits is found to be elliptical as witnessed in Figures 4(b) and 4(c). We estimate the equivalent diameter of the elliptical-shaped pits by using the following formula (Islam et al., 2024):

$$d = \sqrt{ab}. (19)$$

Here, *d*, *a* and *b* are the equivalent diameter of the xylem pit, major and minor axes of the elliptical-shaped pit, respectively. The values of *a* and *b* are measured using ImageJ software.

A closer scrutiny of figures 4(b) and 4(c) reveals that the pits on the root-side xylem walls are comparatively smaller than those on the shoot side. The equivalent diameter of xylem pit d on the root side ranges from 0.881 to 1.751  $\mu$ m, while the same varies from 1.366 to 2.471  $\mu$ m on the shoot side. The distribution of equivalent diameter of xylem wall pits for both root and shoot sides are depicted in figures 4(d) and 4(e), respectively. Also, we calculate the weighted arithmetic average equivalent diameter  $(d_{WA})$  of xylem pits for root and shoot sides by using the following equation (Krejčí & Stoklasa 2018):

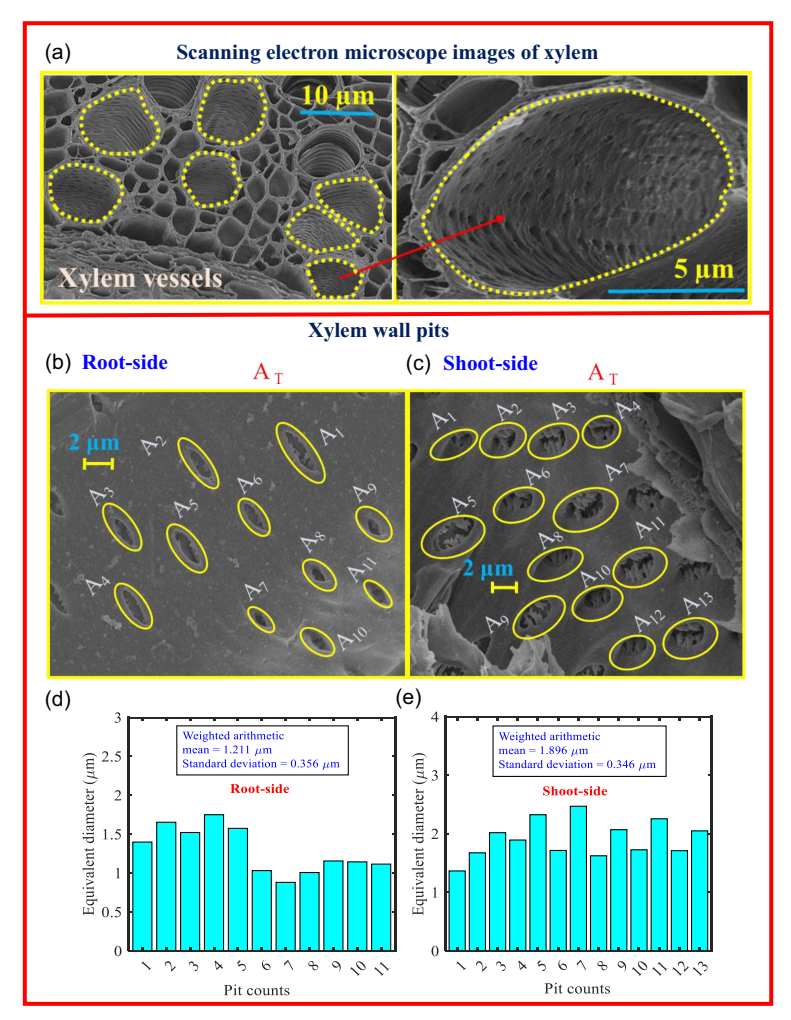


**Figure 4.** (a) Representative SEM images of xylem vessels of Brassica juncea alongside an enlarged view of xylem. Plot demonstrating the xylem wall pit distributions in (b) root side and (c) shoot side of Brassica juncea obtained from SEM. Distributions of the size of the elliptical-shaped pits are shown in (d) root side and (e) shoot side of Brassica juncea.

$$d_{\text{WA}} = \frac{\sum_{i=1}^{n} w_i d_i}{\sum_{i=1}^{n} w_i},$$
(20)

where  $w_i$  and  $d_i$  are the fractional weight and arithmetic mean diameter for a 1  $\mu$ m interval of the distribution, respectively. The interval of the distribution is indexed by i. The value of  $d_{WA}$  for root- and shoot-side xylem wall pits are found to be  $1.211 \pm 0.356 \ \mu$ m and  $1.896 \pm 0.346 \ \mu$ m, respectively.

To estimate the porosity of the xylem wall (pitted porous wall), we calculate the rectangular area  $(A_T)$  of the images shown in Figures 4(b) and 4(c) by enclosing the pits. We also calculate the total pit area  $(\sum A_i)$  in the root and shoot sides. Thus, the porosity  $(\epsilon)$  of the xylem wall can be evaluated using the following formula:

$$\epsilon = \frac{\sum A_i}{A_T}.\tag{21}$$

We estimate the porosity of the xylem wall for both the root and shoot sides of the plant as 0.035 and 0.140, respectively. Finally, we determine the permeability (k) of the pitted porous wall based on

the minimum and maximum equivalent diameters of pits (cf. Figures 4d and 4e). Note that for the calculation of the pitted porous wall permeability, we consider minimum and maximum porosity of elliptical cylindrical pits, and appeal to the Kozeny–Carman equation for cylindrical pores (Schulz et al., 2019) given as

$$k = \frac{d^2}{80} \frac{\epsilon^3}{(1 - \epsilon)^2}.$$
 (22)

It is worth mentioning here that the range of permeability of the pitted porous wall is obtained as  $10^{-18}$  m<sup>2</sup> to  $10^{-15}$  m<sup>2</sup>.

### 3. Results and discussion

In the current study, we consider a two-dimensional configuration of the xylem vessel, as discussed in § 2.2, to estimate nutrient transport through the vessel and to assess the cooperative-correlative effect of ionic nutrient transport on *in situ* electrical energy generation in plants. It is worth adding here that *in situ* electrical energy generation helps bioregulation in plants. To explore this, we estimate the flow velocity of ionic nutrients, average outward radial convective flux, radial flow efficiency, flow-induced electric potential generation inside the plant, hydraulic power, electrical power, specific hydraulic conductivity and electrical conductivity in the xylem vessels. We estimate these parameters for the window of experimentally measured xylem wall porosity, permeability and lumen diameter, as discussed in § 2.3.

In all the cases, the thickness (t) of the pitted porous wall of the xylem vessel is maintained constant as  $t = 1 \mu m$  (Li et al., 2016). We set the inlet root-side reservoir pressure to maintain the pressure gradient (according to the reported experimental results) in the xylem vessel with a shoot-side reservoir pressure of 0 Pa. The previous experimental evidence underscores that the xylem pressure gradient ranges from 0.1 to 20 MPa m<sup>-1</sup> among various plant species (Hellkvist et al.1974). Thus, following this reported data, we consider the range of root-side pressure and a constant shoot-side pressure as 10 to 50 Pa and 0 Pa, respectively, for the xylem length of 55  $\mu$ m for the mentioned range of pressure gradient.

### 3.1. Effect of xylem wall porosity and permeability on the outward radial ionic convective flux

The radial transport of ionic nutrient solutions among the adjacent xylem vessels plays a crucial role in ensuring plant survival under drought stress. It may be mentioned here that the radial transport is largely influenced by the porosity and permeability of the porous pit structures of the xylem walls, which regulate the radial flux of nutrients. In Figures 5(a)-5(d), we demonstrate the average outward radial convective flux  $\int_{CS} \rho(u_r \cdot \boldsymbol{n}) dA$  for potassium and sulphate ions through the porous wall versus rootside inlet pressure. The plots are depicted for varying porosity and permeability of the pitted porous wall. It is evident that radial convective flux of both potassium and sulphate ions increases with the increase in wall porosity (cf. Figure 5a, b). This is because the fractional void regions increase at higher porosity, offering additional pathways for the ionic nutrients to radially move out through the porous wall of the xylem vessel. This effect is more prominent at higher inlet pressure for sulphate ion, attributed primarily to the enhanced strength of advection. The augmented advection aids in overcoming the electrostatic repulsion between  $SO_4^{2-}$  ions and the negatively charged xylem wall, pushing more  $SO_4^{2-}$  ions radially outward of the xylem vessel through the wall. However, the stronger electrostatic attraction between K<sup>+</sup> ions and the negatively charged xylem wall limits the increasing rate of average outward radial convective flux for potassium ions with increasing inlet pressure. Similarly, the average radial convective flux for both ionic nutrients increase with higher wall permeability of the xylem vessel (cf. Figures 5c and 5d). It is attributed to the enhanced conductance of the radial flow with higher permeability of the xylem wall, which promotes the radial transport of an ionic nutrient solution through the walls. The foregoing analysis signifies the importance of radial transport among the adjacent xylem vessels of the plants for their adequate growth and long-term survival. However, under the severe drought stressed condition, the pressure inside the xylem vessels significantly drops, which, in turn, reduces the radial transport of

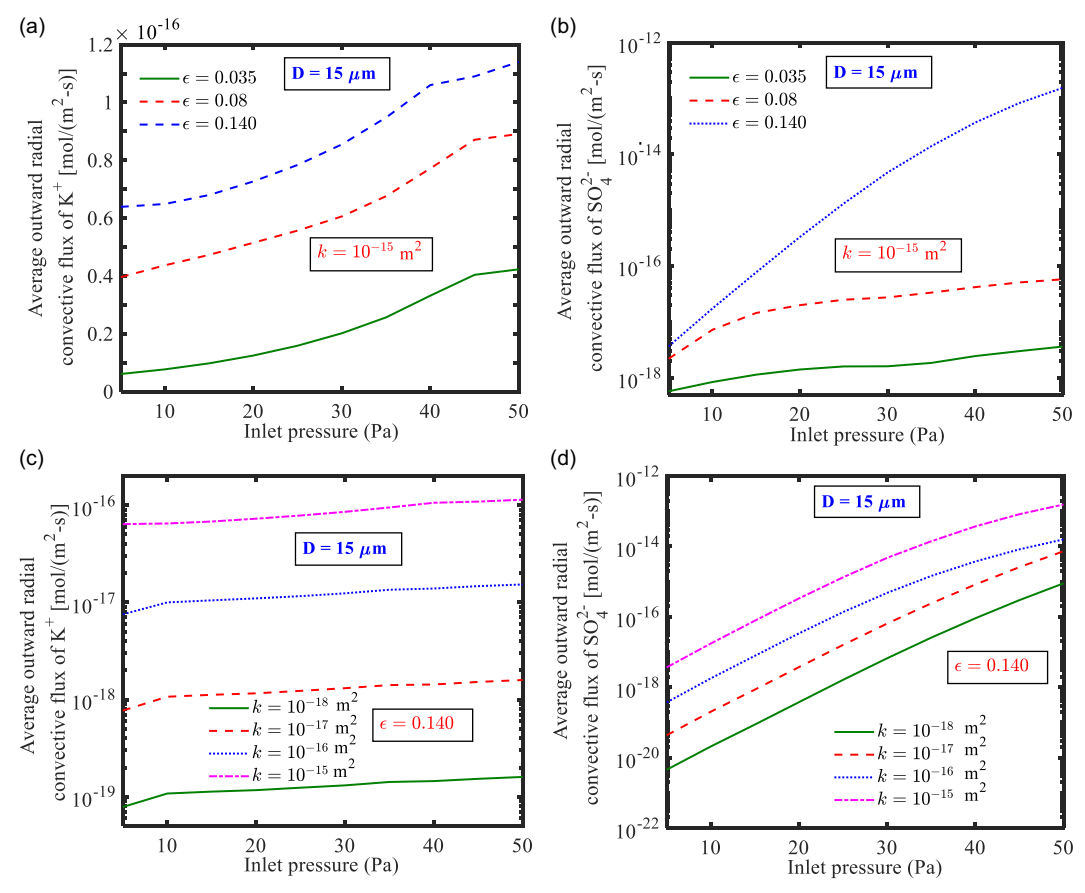


**Figure 5.** Plot depicting the variation in average outward radial convective flux of potassium  $(K^+)$  and sulphate  $(SO_4^{2-})$  ions versus root-side inlet pressure. The variations are depicted for different morphological parameters of xylem vessel: (a),(b) for different values of porosity and (c),(d) for different values of permeability. The xylem is modelled with pitted porous wall having lumen diameter  $D = 15 \mu m$ .

ionic nutrients. The underlying phenomenon becomes detrimental for plant survivability and ultimately leads to plants' death at draught stress condition.

### 3.2. Effect of xylem lumen diameter on nutrient transport and energy generation

The SEM imaging illustrated in Figure 6(a) depicts the lumen diameter distribution in the vascular bundle of *B. juncea*. From this micro-level image, we estimate that the lumen diameter approximately ranges from 5 to 15  $\mu$ m. Accordingly, we show in Figure 6(b) the flow field contours inside the xylem vessel for the experimentally calculated range of lumen diameter. It is observed from Figure 6(b) that the flow velocity follows an increasing trend with an increase in the magnitude of the lumen diameter. This observation is attributed to the enhancement in mass flow rate of the ionic nutrient as the cross-sectional area increases with a larger lumen diameter. The increased mass flow rate intensifies the flow field at a larger lumen diameter during the flow of incompressible aqueous ionic solution through xylem vessels, as witnessed by the flow field contours depicted in Figure 6(b).

From (15), it is evident that the net ionic current strongly depends on the convective flux  $(=u_zc_i)$ . In an effort to look into the underlying physics of energy generation, we illustrate the convective flux contours of  $K^+$  in Figure 6(c) for two different values of the lumen diameter for lower (left) and higher (right) root-side pressure. We observe that the convective flux enhances with an increase in lumen diameter for both low and high root-side pressures. We attribute this observation to the augmentation in axial

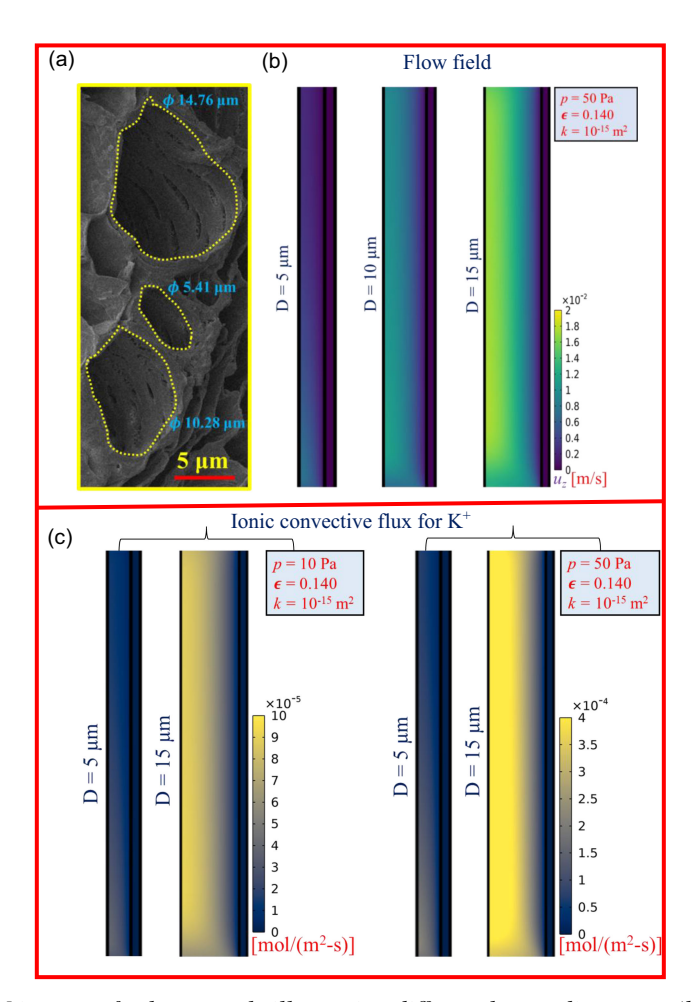


**Figure 6.** (a) SEM images of xylem vessels illustrating different lumen diameters. (b) Contours of axial flow velocity simulated for three different values of lumen diameters:  $5 \mu m$  (left),  $10 \mu m$  (middle) and  $15 \mu m$  (right). (c) Contours of the convective flux for  $K^+$  at different lumen diameter when root-side pressure is 10 Pa (left) and 50 Pa (right). The other parameters being  $\epsilon = 0.140$ ,  $k = 10^{-15} m^2$ , and root-side inlet pressure is equal to 50 Pa.

flow strength (cf. Figure 6b) and  $K^+$  concentration as the lumen diameter increases. The increase in  $K^+$  concentration with lumen diameter is mainly due to the higher strength of the convection-dominated ionic transport in the prevailing situation, as the ionic Péclét number exceeds unity ( $\sim 100$ ). For the same reason, higher root-side pressure allows greater convective flux of  $K^+$  concentration owing to the greater flow velocity of the ionic nutrient solution. Note that the increased  $K^+$  concentration in plants is deemed pertinent to enhance the stomatal conductance and transpiration rates of water through leaves (Sperling et al., 2024), which, in turn, ultimately promotes plant growth and yield. Therefore, we can infer that the increased flux of  $K^+$  in the lumen with larger diameter will lead to optimal growth of plants because of the enhancement in photosynthetic activity owing to the augmented stomatal conductance (Sperling et al., 2024).

The efficiency of radial flux, as expressed in (14), is related to the resistance  $(F_m = \Delta p_m/Q_m)$  offered to the underlying transport through the xylem wall. Quite notably, the efficiency of radial flux thus depends on the geometrical configuration of the xylem wall considered in the model. To investigate this important fluidic functionality of the xylem vessel, we demonstrate the variation in flow resistance provided by xylem wall versus root-side inlet pressure considering two different models (solid wall and

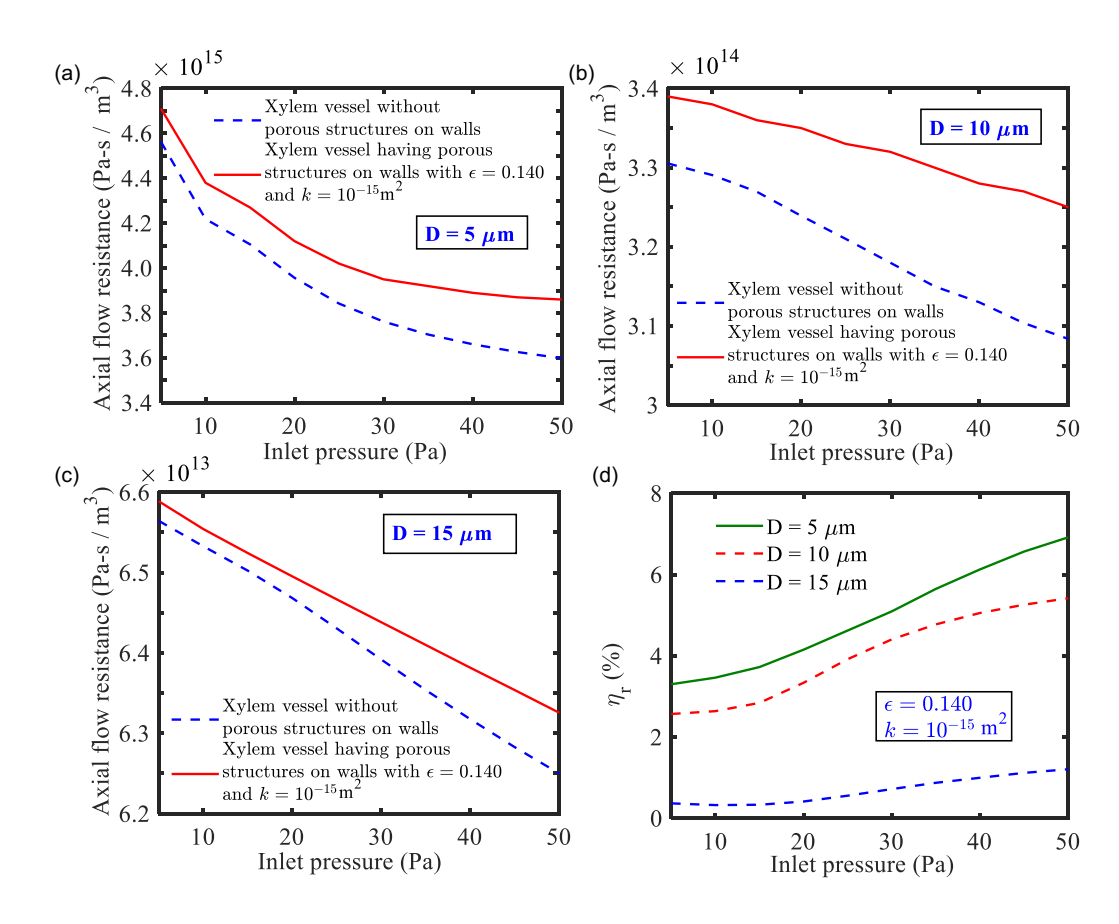


**Figure 7.** Plot showing the comparison of flow resistance (calculated from numerical simulations) through xylem vessel having a solid wall and pitted porous wall versus root-side inlet pressure for different values of lumen diameter: (a)  $D = 5 \mu m$ ; (b)  $D = 10 \mu m$ ; and (c)  $D = 15 \mu m$ . (d) Variation in radial flow efficiency  $(\eta_r)$  with respect to root-side inlet pressure, obtained for different lumen diameter. The other parameters considered are  $\epsilon = 0.140$  and  $k = 10^{-15}$  m<sup>2</sup>.

porous wall), as shown in Figures 7(a)–7(c). The variations are depicted for three different values of lumen diameter D=5,10 and 15  $\mu m$ . We observe that flow resistance decreases with an increase in root-side inlet pressures. It is attributed to the rate of increase in net throughput owing to the higher pressure drop as well as concentration gradient induced flow actuation. Moreover, the flow resistance predicted by the pitted porous wall model is found to be higher than that of the solid wall model. Thus, for a given pressure difference, the axial flow rate calculated by the present model is expected to be less than that predicted by the solid wall model. It may be mentioned here that the contribution of radial transport through the pitted porous wall reduces the axial flow velocity through the xylem vessel upon satisfying the mass conservation constraint. Interestingly, the flow resistance decreases by an order of magnitude with an increase in lumen diameter. This reduction in flow resistance can be attributed to the increase in lumen diameter according to the Hagen–Poiseuille law ( $h_f \propto 1/D$ ). Furthermore, the solid wall model (without a pitted porous wall) greatly under-predicts the axial flow resistance at higher inlet pressure, particularly for smaller lumen diameters. The axial flow resistance percentage under-prediction ranges from 3.14 % to 6.78 % and 0.37 % to 1.19 % for 5  $\mu$ m and 15  $\mu$ m lumen diameters, respectively, within the stated inlet pressure range.

The flow resistance follows ideal Hagen–Poiseuille law at larger lumen diameters due to the minimal effect of ionic concentration gradient on the underlying flow, resulting from a decrease in electric-double layer thickness. Also, the variation in radial efficiency with root-side inlet pressure is depicted

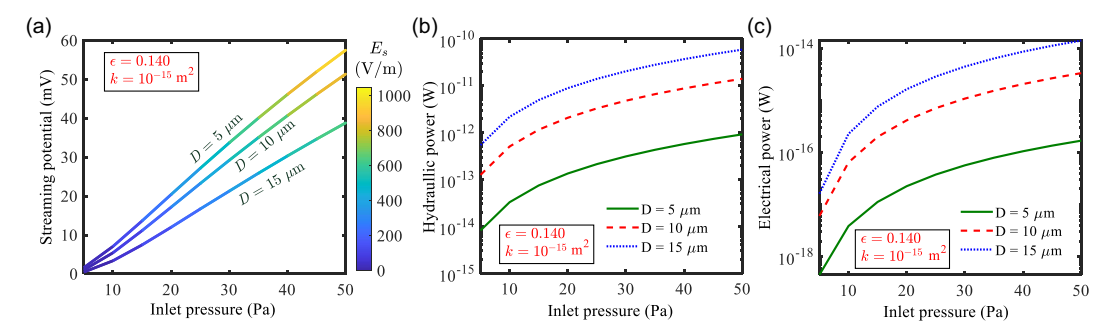


**Figure 8.** Variation in (a) induced electric potential and in situ electric field (colour-coded), (b) hydraulic power and (c) electrical power at different lumen diameter by changing the root-side inlet pressure. The other parameters considered are  $\epsilon = 0.140$  and  $k = 10^{-15}$  m<sup>2</sup>.

in Figure 7(d) for the different values of lumen diameter. It is observed that the radial flow efficiency increases with root-side inlet pressure. The highly pressurised transport through xylem vessels at elevated root-side pressure improves the radial flow, which, in turn, enhances the radial flow efficiency. Moreover, the radial flow efficiency reduces with an increase in the lumen diameter. Note that an increase in axial flow velocity with increasing the lumen diameter for a given driving force (cf. Figure 6b) is expected to render smaller radial flow velocity through the pitted porous wall of the xylem to satisfy the mass conservation constraints. Thus, attenuation of radial flow velocity at larger lumen diameter reduces the radial flow efficiency as witnessed in Figure 7(d). Reducing the lumen diameter from 15  $\mu$ m to 5  $\mu$ m increases radial efficiency by 471.9 %–793.2 % in the stated inlet pressure range. Note that the higher radial flow efficiency in narrower xylem is deemed beneficial as it supports the plants' survivability under the drought-induced stressed situation.

As the diameter of xylem vessels significantly impacts the bioactivities in plants (Schreiber et al., 2015), we make an effort to unveil the correlation between in situ electrical energy generation characteristics and bioregulation in plants for different values of lumen diameter. To this end, we first present in Figure 8(a) the variation of in situ electric potential difference along with the electric field (colour-coded) generated inside the plants versus root-side inlet pressure for the chosen window of lumen diameters. It can be visualised that the accumulation of more counter-ions in the shoot side (transport takes place from the root side to the shoot side) due to the higher convective strength with increase in the root-side inlet pressure augments the electric potential. Notably, a significant reduction in the electric potential is observed with an increase in lumen diameter. This observation can be attributed to the formation of thinner electrical-double layer at the walls of larger xylem vessels, which restricts the displacement of counter-ions from upstream (root side) to downstream (shoot side) of the vessel (cf. Figure 6c). This effect ultimately culminates in a smaller potential difference across the xylem vessels with larger lumen diameter. Reported inferences suggest that the plants with larger xylem vessels show enhancement in growth parameters, such as height, hydraulic conductivity, photosynthetic activity, CO<sub>2</sub> fixation and transpiration rate (Manhães et al. 2022; Qaderi et al., 2019; Schreiber et al., 2015; Yugang & Hongyi, 2013). In this study, we obtain a higher value of electric potential for smaller lumen diameter. This observation suggests that the electrical potential is not the sole factor influencing plant growth. It is worth mentioning here that the order of in situ electric field observed in our numerical analysis aligns with the reported experimental evidence as well (Venkata Mohan & Yeruva, 2023).

The effect of lumen diameter on hydraulic power is presented in Figure 8(b). The variations are depicted for different values of the root-side inlet pressure. We observe that the hydraulic power is enhanced with an increase in root-side pressure, attributed primarily to the increase in nutrient mass flow rate. Notably, an increase in lumen diameter augments the hydraulic power by nearly an order of magnitude for a given root-side pressure. It is attributed to the dependency of flow rate on the square of the lumen diameter according to the Hagen–Poiseuille law. Additionally, a significant reduction in axial flow resistance (cf. Figures 7a-7c) synonymously improves the axial flow velocity with an increase

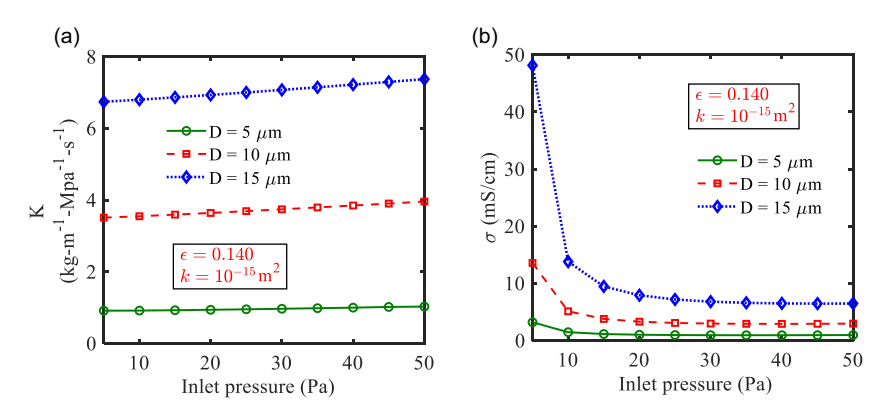


**Figure 9.** Plot showing the variation of (a) specific hydraulic conductivity (K) and (b) electrical conductivity ( $\sigma$ ) in the window of root-side inlet pressure at different lumen diameters. The other parameters being  $\epsilon = 0.140$  and  $k = 10^{-15}$  m<sup>2</sup>.

in lumen diameter. Therefore, a reduction in axial flow resistance ( $h_f \propto 1/D$ ) together with larger flow pathway area with increasing lumen diameter increases the axial flow rate ( $Q = \frac{\pi}{4}D^2u_{zAvg}$ ) and simultaneously improves the hydraulic power (=  $Q\Delta p$ ). The increased hydraulic power in larger xylem vessels results in the transport of more ionic nutrients (both co- and counter-ions) with higher flow rate. This augmented nutrient flow in the plants promotes various bioactivities, such as stomatal conductivity, transpiration, photosynthesis, early flowering, etc. (Venkata Mohan & Yeruva, 2023). Thus, plants composed of larger xylem vessels showcase a rapid growth and development (Manhães et al. 2022; Qaderi et al., 2019; Schreiber et al., 2015; Yugang & Hongyi, 2013), primarily because of the higher nutrient transport through vasculature.

Since the electrical stimulation modulates the bioactivities in plants (Venkata Mohan & Yeruva, 2023), there may be a possibility that electrical energy induced in the xylem vessel influences metabolic regulation in plants. Thus, we estimate the electrical power generation  $(=I_z V_S)$  and present the variation of the same with root-side pressure in Figure 8(c). The variations are depicted for different values of lumen diameter and root-side inlet pressure. A substantial increase in electrical power is evident with an increase in root-side inlet pressure and this is mainly due to the significant increase in ionic convective flux (cf. Figure 6c). Similarly, an augmentation in ionic convective flux in larger lumen diameter causes prominently higher electrical power to develop inside the plant. This observation suggests that in situ electrical energy in plants can be augmented by supplying more ionic nutrients to the growing media. This electrical power may act as an inherent electrical stimulation for plants to perform a variety of bioactivities (Venkata Mohan & Yeruva, 2023). Notably, the electrical power generation follows a reverse trend than that of the induced electric potential with increase in lumen diameter. This observation essentially demonstrates that plant growth under the development of an inherent electrical field in the vasculature is not solely dependent on the potential difference, but also depends on the net flow of ionic current in the xylem vessels. Thus, increased in situ electrical energy in larger xylem vessels is deemed beneficial for the plant height, chlorophyll content, number of primary nodes, carbohydrate contents, CO<sub>2</sub> fixation and upregulation of relative gene expression owing to enhanced ionic nutrient transport, as evident from the reported work (Venkata Mohan & Yeruva, 2023).

To quantify the axial flow efficacy of the xylem vessels, we define the specific hydraulic conductivity of the xylem. This parameter is interpreted as the ratio of the mass flow rate of nutrient solution in the xylem vessel per unit pressure gradient as expressed in (17). We plot, in Figure 9(a), the variation of specific hydraulic conductivity with root-side inlet pressure. The variations are shown for different values of lumen diameter. It is observed that the root-side pressure has minimal effect on the specific hydraulic conductivity at lower lumen diameter. The increased throughput maintains almost a constant ratio of specific hydraulic conductivity with increase in root-side inlet pressure at a lower range of lumen diameter. However, for bigger xylem vessels, a slight increase in specific hydraulic conductivity

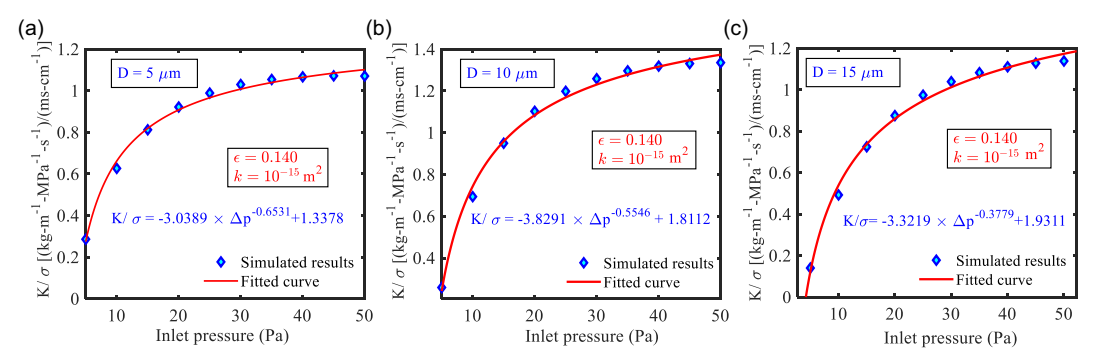


**Figure 10.** Plots depicting the variation of specific hydraulic conductivity to electrical conductivity ratio  $(K/\sigma)$  versus root-side inlet pressure for different diameters of xylem lumen: (a) 5  $\mu$ m; (b) 10  $\mu$ m; and (c) 15  $\mu$ m. The best fitted curve fitted curve is also portrayed in the respective figure. The other parameters considered are  $\epsilon = 0.140$  and  $k = 10^{-15}$  m<sup>2</sup>.

is visible towards higher root-side pressure due to significant increase in flow velocity (cf. Figure 6*b*). Interestingly, the specific hydraulic conductivity of the xylem vessel increases with an increase in its diameter. It is attributed to the higher mass flow rate of nutrient solution in the larger xylem vessel caused by the increased flow velocity at the same value of the root-side inlet pressure (cf. Figure 6*b*). The higher specific hydraulic conductivity of larger xylem vessels makes it possible to transport the ionic nutrient solution more efficiently, supporting appreciable plant growth (Manhães et al. 2022; Qaderi et al., 2019; Schreiber et al., 2015; Yugang & Hongyi, 2013).

The electrical conductivity, as expressed in (18), is also a crucial parameter typically used to describe plant health. This parameter directly governs the availability of ionic nutrients to the xylem vessels and becomes an indicator of osmotic stress (Carmo et al., 2024). Figure 9(b) depicts the change in electrical conductivity with root-side inlet pressure obtained for different values of lumen diameter. The electrical conductivity is found to decrease substantially with an increase in lower root-side inlet pressure for its lower range. It is due to the dominance of the increase in electric potential difference with the increase in this range of a lower root-side pressure (cf. Figure 8a). However, a mild reduction in electrical conductivity is evident for higher root-side pressure. The substantial increase in ionic current owing to enhanced ionic convective flux at a larger root-side pressure enables a greater rate of augmentation of  $V_sA$  appearing in the denominator of (18). Hence, the coupled effect of enhanced in situ electric potential development and substantial increase in ionic current at larger root-side pressure allows a milder reduction in electrical conductivity. It is also seen that the electrical conductivity is significantly increased with the lumen diameter. This observation is attributed to the coupled effect of increase in ionic current and decrease in induced electric potential difference (cf. Figure 8a) at the larger lumen diameter. Here, it is observed that the larger lumen diameter allows higher ionic convective flux to set in (cf. Figure 6c) so that the net ionic current becomes higher. However, it is worth mentioning in this context here that a higher electrical conductivity is not beneficial for the plants as it indicates salinity stress due to the presence of more salts (Cha et al., 2021). In contrast, a smaller value of electrical conductivity denotes nutrient deficiency in plants (Carmo et al., 2024). Thus, in the forthcoming section, we present the variation of the ratio of specific hydraulic conductivity to the electrical conductivity  $(K/\sigma)$  of the xylem vessel to estimate the relative importance of these two flow parameters on overall growth of the plants.

We present in Figures 10(a)-10(c) how the ratio of specific hydraulic conductivity and electrical conductivity  $(K/\sigma)$  varies with the root-side inlet pressure for different values of lumen diameter. It is evident that the variation in  $K/\sigma$  with pressure drop in the xylem vessel follows approximately a power law relation  $(a\Delta p^b + c)$  having a correlation coefficient value greater than 0.99. For all the values of lumen diameter considered, the ratio is found to be less than unity at a lower root-side inlet pressure. This is attributed to the existence of a substantially higher electrical conductivity value (cf. Figure 9b)

as compared with the specific hydraulic conductivity (cf. Figure 9a) at lower values of root-side inlet pressure. It can be correlated to the availability of more ionic nutrients or salts in the nutrient solution at a lower range of root-side inlet pressure in the xylem vessel. The prevailing situation is reminiscent of plants undergoing drought stress, enabling a lower pressure difference to act across the xylem vessel (Jansen et al., 2003), and results in a lower predication of  $K/\sigma$ . Hence, we can say that the lower value of  $K/\sigma$  is one of the indications of drought stress. Further, increasing the root-side inlet pressure augments the value of  $K/\sigma$ . We attribute this observation to the combined effect of increased specific hydraulic conductivity and decrease in electrical conductivity of the xylem vessel at a higher range of the root-side inlet pressure (cf. Figure 9a, b). We can further substantiate the underlying discussion on the variation of the  $K/\sigma$  ratio in conjunction with the salt stress condition as follows. For wheat crop, the control condition is approximately  $K = 1.2 \text{ Kg m}^{-1} \text{ s}^{-1} \text{ MPa}^{-1}$  and  $\sigma = 3 \text{ mS cm}^{-1}$ . However, the high salt stress condition shows nearly  $K = 0.1 \text{ Kg m}^{-1} \text{ s}^{-1} \text{ MPa}^{-1}$  and  $\sigma = 10 \text{ mS cm}^{-1}$  (Fu et al., 2024; Thi et al., 2017). For a wheat plant, therefore, we obtain the value of  $K/\sigma$  as approximately 0.4 and 0.01 (Kg m<sup>-1</sup> s<sup>-1</sup> MPa<sup>-1</sup> (mS cm<sup>-1</sup>)) for control and high salt stressed conditions, respectively. We can clearly observe that the higher  $K/\sigma$  ratio signifies a healthy condition of plant (control condition). In contrast, a lower value of  $K/\sigma$  is evident when plant is undergoing severe salt stressed condition. From the aforementioned discussion, we can infer that the ratio of specific hydraulic conductivity and electrical conductivity is a suitable index for describing the plant health.

It may be mention here that the  $K/\sigma$  ratio of the xylem vessel is dependent on the pressure drop in the xylem following the relation as  $K/\sigma = a\Delta p^b + c$ . Here, the constants 'a', 'b' and 'c' are several functions of the lumen diameter described as

$$a = eD^{3} + fD^{2} + gD + h, (23)$$

where e = -0.0032, f = 0.1224, g = -1.4435 and h = 1.5103;

$$b = pD^2 + qD + r, (24)$$

where p = 0.0017, q = -0.0070 and r = -0.6619;

$$c = mD^n + s, (25)$$

where m = -11.4678, n = -1.763 and s = 2.0111.

Having a closer look at the aforementioned equations, we find that the variation of  $K/\sigma$  is non-monotonic with the lumen diameter. Therefore, we find a non-monotonic variation of constant, a, with the change in lumen diameter (cf. (23)). This observation is attributed to the following. First, the rate of change in electrical conductivity with the lumen diameter in the window of pressure drop. Second, increasing nature of K and  $\sigma$  with lumen diameter (cf. Figure 9a, b). Hence, increasing the value of both K and  $\sigma$  allows non-monotonic trend of  $K/\sigma$  with lumen diameter in the considered range of pressure drop.

### 4. Conclusions

In this endeavour, we investigated the influence of *in situ* electrical energy on plant's bioregulation. We showed that the electrical energy is generated within the plant from the inherent flow of ionic nutrient solution through xylem vessels. We used scanning electron microscopy of the vascular bundles of *Brassica juncea* to visualise the lumen diameter and pit configurations on the xylem walls. We developed a two-dimensional model of the xylem vessel using experimentally captured geometrical parameters to simulate the flow field, ionic concentration distribution and electric potential fields within the plant. Accounting for the effect of flow-induced structural deformation of the soft xylem wall on the underlying flow, we employed a two-way coupled fluid–structure interaction to determine the flow parameters governing nutrient transport. We systematically investigated the development of axial flow field, axial and radial ionic convective flux, radial flow efficiency, *in situ* electric potential difference, hydraulic power, electrical power, and electrical conductivity for the experimentally measured window of xylem geometrical parameters and physically justified range of root-side inlet pressure. It is found that the

radial convective flux follows an increasing trend for both cationic and anionic nutrient components with increasing pitted porous wall porosity and permeability. We revealed that the lumen diameter substantially augments the ionic convective flux and the flow field. Interestingly, the rate of reduction in axial flow resistance with root-side inlet pressure is found to be highly dependent on the lumen diameter. For smaller lumen diameter, the rate of reduction in axial flow resistance with root-side inlet pressure is seen to be nonlinear. However, in larger lumen, the reduction in flow resistance with increasing root-side inlet pressure follows a nearly linear trend, adhering to the Hagen-Poiseuille law. We found that the axial flow resistance drops with increasing lumen diameter, indicating a greater radial flow resistance. Consistent with this observation on lumen diameter modulated alteration in axial flow resistance, we stipulated that the larger lumen diameter impedes the radial transport and results in lower radial nutrient flow efficiency – a situation that becomes detrimental for the survival of plants during drought-induced stress. Intriguingly, we established that in situ electric potential difference decreases with increasing the lumen diameter. Despite a reduction in the development of electric potential within the plant with larger lumen diameter, we found that increasing lumen diameter improves both hydraulic power and electrical power. This finding underscores that the plant's growth under the influence of an inherent electric field depends not only on the electric potential difference (inevitably associated with ionic nutrient flow through the xylem vessel), but also on electrical power. We argued that the combined effect of augmented electrical and hydraulic power may lead to an enhancement in a variety of bioactivity in plants with larger xylem vessels. Furthermore, we explored that the specific hydraulic conductivity and electrical conductivity augments with the lumen diameter, attributed to the increased ionic nutrient flow through the larger xylem vessels. We have established that the ratio of specific hydraulic conductivity to electrical conductivity  $(K/\sigma)$  is an index of plant health. Finding evidence of non-monotonic dependence of  $K/\sigma$  on lumen diameter, we also unveiled that  $K/\sigma$  follows an increasing trend with the increase in root-side pressure. We believe that the findings of this research endeavour will provide a comprehensive understanding of electrohydrodynamic regulation of bioactivities in plants that act as a possible electrical energy generation source.

Acknowledgments. We would like to extend our sincere gratitude to the Central Instruments Facility (CIF) of IIT Guwahati for providing access to the scanning electron microscope imaging facility.

**Author contribution. J.K.:** Conceptualisation, Methodology, Software, Investigation, Writing - Original Draft, Visualisation, Experiments. **S. K.M.:** Conceptualisation, Methodology, Software, Experiments, Formal analysis, Writing - Original Draft. **P.K.M.:** Conceptualisation, Formal analysis, Visualisation, Supervision, Project administration, Funding acquisition, Writing - Review & Editing.

**Funding statement.** P.K.M. gratefully acknowledges the financial support provided by the SERB (DST), India, through project no. CRG/2022/000762. S.K.M. acknowledges the financial support provided by the National Post-Doctoral Fellowship (N-PDF), SERB, with Reference No. PDF/2023/002072.

Ethical standards. The research meets all ethical guidelines, including adherence to the legal requirements of the study country.

Data availability statement. The authors declare that all data used in the work are available in this paper.

Competing interests. The authors declare no competing financial interest.

### Appendix A. Calculation of grid convergence index (GCI)

To calculate the grid convergence index (GCI), we first define the average mesh size (H) for the two-dimensional computational domain, as chosen in this analysis. The average mesh size is estimated using the following expression:

Key variables $(f)$	Average axial velocity at the mid cross-section of xylem, $w \text{ (m s}^{-1})$
$\overline{N_1, N_2, N_3}$	184 216, 69 252, 29 359
$R_{21}$	1.63
$R_{32}$	1.54
$f_1$	0.006715
$f_2$	0.006719
$f_3$	0.006796
P	6.8122
$e_a^{21}$ (%)	0.0611
$e_{a}^{21}$ (%) $e_{ext}^{21}$ (%)	0.015
$GCI_{fine}^{21}$ (%)	0.00284
$GCI_{fine}^{32}(\%)$ $GCI_{fine}^{32}$	0.07911
$rac{G ilde{C}I_{ extit{fine}}^{32}}{R_{21}^PGCI_{ extit{fine}}^{21}}$	0.9994≈1

**Table 1.** Calculation of the error in discretization

$$H = \left[\frac{1}{N_T} \sum_{i=1}^{N_T} (\Delta A_n)\right]^{1/2}.$$
 (26)

Here,  $N_T$  and  $\Delta A_n$  are the total number of mesh elements and the total area of the meshed domain, respectively.

It is reported that the desirable grid refinement factor,  $R = H_{coarse}/H_{fine}$ , should be greater than 1.3. Hence, in our study, the values of  $R_{21} = H_2/H_1$  and  $R_{32} = H_3/H_2$  are maintained to be greater than 1.3, where  $H_1 < H_2 < H_3$ . Now, the apparent order of convergence, P, is calculated by applying the following expression:

$$P = \frac{1}{\ln(R_{21})} \left| \ln \left| \delta_{32} / \delta_{21} \right| + q(P) \right|, \tag{27}$$

$$q(P) = \ln\left(\frac{R_{21}^P - s}{R_{32}^P - s}\right),\tag{28}$$

where  $s = 1 \cdot \text{sign}(\delta_{32}/\delta_{21})$ , in which  $\delta_{32} = f_3 - f_2$  and  $\delta_{21} = f_2 - f_1$ . It is noteworthy to mention that q(P) = 0 for a constant value of R. Equation (27) is solved by using fixed-point iteration. The extrapolated values of f can be evaluated as

$$f_{ext}^{21} = \left(R_{21}^P f_1 - f_2\right) / \left(R_{21}^P - 1\right). \tag{29}$$

Following similar steps, we estimated  $f_{ext}^{32}$ .

Further, the relative projected error and relative extrapolated error are determined as

$$e_a^{21} = \left| \frac{f_1 - f_2}{f_1} \right|,\tag{30}$$

$$e_{ext}^{21} = \left| \frac{f_{ext}^{12} - f_1}{f_{ext}^{12}} \right|. \tag{31}$$

Thus, the fine-grid convergence index ( $GCI_{fine}$ ) is calculated as

$$GCI_{fine}^{21} = \frac{1.25e_a^{21}}{R_{21}^P - 1}. (32)$$

The values of several parameters calculated during the evaluation of GCI are mentioned in Table 1.

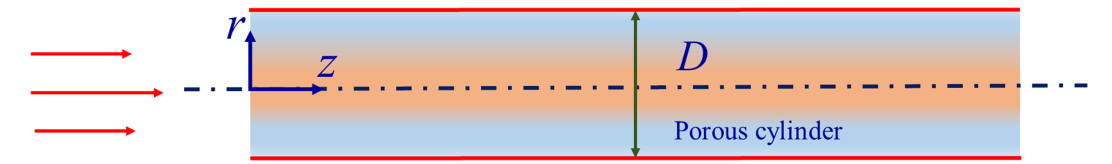


Figure 11. Fully developed flow in a porous microcylinder.

# Appendix B. Benchmarking of porous media flow

The flow through xylem pits, which falls in the low-Reynolds-number regime ( $\text{Re} \ll 1$ ), in the absence of any external forcing can be represented as the flow through a porous microcylinder, as shown in Figure 11. The momentum transport equation describing the underlying low-Reynolds-number flow, consistent with the Darcy model, is written as (Behera et al., 2023)

$$-\frac{\partial p}{\partial z} + \frac{\mu}{\epsilon} \frac{\partial^2 u}{\partial r^2} - \frac{\mu u}{k} = 0,\tag{33}$$

where p,  $\mu$ ,  $\epsilon$ , k and u are the pressure, dynamic viscosity, porosity, permeability and z-component of velocity respectively.

Now, we take an effort to write (33) in its non-dimensional counterpart using the dimensionless variables written as

$$r^* = \frac{r}{D}, z^* = \frac{z}{D}, u^* = \frac{u}{u_{max}}, p^* = \frac{p}{\left(\frac{\mu D u_{max}}{k}\right)}.$$

The dimensionless momentum transport equation reads as

$$-\frac{\partial p^*}{\partial z^*} + \frac{Da}{\epsilon} \frac{\partial^2 u^*}{\partial r^{*2}} - u^* = 0.$$
 (34)

Here,  $Da = \frac{k}{D^2}$  denotes the Darcy number (Awartani & Hamdan, 2005). The complete solution of the (34) is given as follows:

$$u^*(r^*) = C_1 e^{\left(r^* / \sqrt{Da/\epsilon}\right)} + C_2 e^{-\left(r^* / \sqrt{Da/\epsilon}\right)} + \left(-\frac{\partial p^*}{\partial z^*}\right). \tag{35}$$

We apply no-slip conditions at the walls of the micropore essentially to obtain constants  $C_1$  and  $C_2$  appearing in (35) as follows: at  $r^* = \pm 0.5$ ,  $u^*(r^*) = 0$ . On using the constants  $C_1$  and  $C_2$ , we obtain the following expression of the flow velocity:

$$u^{*}\left(r^{*}\right) = \left(-\frac{\partial p^{*}}{\partial z^{*}}\right) \left[\frac{\left(e^{\frac{0.5}{\sqrt{Da/\epsilon}}} + e^{\frac{-0.5}{\sqrt{Da/\epsilon}}}\right) - \left(e^{\frac{r^{*}}{\sqrt{Da/\epsilon}}} + e^{\frac{-r^{*}}{\sqrt{Da/\epsilon}}}\right)}{e^{\frac{0.5}{\sqrt{Da/\epsilon}}} + e^{\frac{-0.5}{\sqrt{Da/\epsilon}}}}\right].$$
(36)

Note that we have used  $u_{max}$  as the reference velocity scale. Hence,  $u^*(=u/u_{max})$  will be equal to 1 at  $r^*=0$ , implicating that the magnitude of non-dimensional pressure gradient  $-\frac{\partial p^*}{\partial z^*}\approx 1$  for the window of Da and  $\epsilon$  pertinent to this analysis. Thus, the final form of non-dimensional axial velocity profile (36) for the flow in a partially porous microcylinder can be represented as

$$u^* (r^*) = \left[ \frac{\left( e^{\frac{0.5}{\sqrt{Da/\epsilon}}} + e^{\frac{-0.5}{\sqrt{Da/\epsilon}}} \right) - \left( e^{\frac{r^*}{\sqrt{Da/\epsilon}}} + e^{\frac{-r^*}{\sqrt{Da/\epsilon}}} \right)}{e^{\frac{0.5}{\sqrt{Da/\epsilon}}} + e^{\frac{-0.5}{\sqrt{Da/\epsilon}}}} \right]. \tag{37}$$

### References

- Awartani, M. M., & Hamdan, M. H. (2005). Fully developed flow through a porous channel bounded by flat plates. Applied Mathematics and Computation, 169, 749–757.
- Behera, P. P., Mehta, S. K., Arun, R. K., & Mondal, P. K. (2023). Solute imbibition in paper strip: Pore-scale insights into the concentration-dependent permeability. *Physics of Fluids*, 35(12), 122007.
- Brodersen, C. R., Roddy, A. B., Wason, J. W., & McElrone, A. J. (2019). Functional status of xylem through time. *Annual Review of Plant Biology*, 70, 407–433.
- Cabrita, P., Thorpe, M., & Huber, G. (2013). Hydrodynamics of steady state phloem transport with radial leakage of solute. Frontiers in Plant Science, 4, 531.
- Carmo, A. P. M.do, Freitas, M. S. M., Machado, L. C., & de Carvalho, A. J. C. (2024). Electrical conductivity of nutrient solutions affects the growth, nutrient levels, and content and composition of essential oils of Acmella oleracea (L.) R. K. Jansen from southeastern Brazil. *Journal of Agriculture and Food Research*, 15, 100968.
- Celik, I. B., Ghia, U., Roache, P. J., Freitas, C. J., Coleman, H., & Raad, P. E. (2008). Procedure for estimation and reporting of uncertainty due to discretization in CFD applications. *Journal of Fluids Engineering, Transactions of the ASME*, 130(7), 0780011–0780014.
- Cha, S. J., Park, H. J., Kwon, S. J., Lee, J. K., & Park, J. H. (2021). Early detection of plant stress using the internal electrical conductivity of Capsicum annuum in response to temperature and salinity stress. *Plant Growth Regulation*, 95(3), 371–380.
- Chen, Q., Xu, F., Ai, Q., & Zhang, L. (2015). Hydrodynamic model and flow resistance characteristics of plant vessel wall thickenings. *Transactions of the Chinese Society of Agricultural Engineering*, 31(19), 1–8.
- Cosgrove, D. J. (1993). Water uptake by growing cells: An assessment of the controlling roles of wall relaxation, solute uptake, and hydraulic conductance. *International Journal of Plant Sciences*, 154(1), 10–21.
- De Boer, A. H., & Volkov, V. (2003). Logistics of water and salt transport through the plant: Structure and functioning of the xylem. *Plant, Cell and Environment*, 26(1), 87–101.
- de Toledo, G. R. A., Parise, A. G., Simmi, F. Z., & Souza, G. M. (2019). Plant electrome: The electrical dimension of plant life. *Theoretical and Experimental Plant Physiology*, 31(1), 21–46.
- Farquhar, G. D., & Field, C. D. (1971). Transpiration-linked short-circuit currents in the xylem of a liana. *Journal of Experimental Botany*, 22(4), 818–829.
- Fu, Y., Li, P., Si, Z., Ma, S., & Gao, Y. (2024). Seeds priming with melatonin improves root hydraulic conductivity of wheat varieties under drought, salinity, and combined stress. *International Journal of Molecular Sciences*, 25(9), 5055.
- Graziana, A., Ranjeva, R., & Teissié, J. (1990). External electric fields stimulate the electrogenic calcium/Sodium exchange in plant protoplasts. *Biochemistry*, 29(36), 8313–8318.
- Guha, A., Bandyopadhyay, S., Bakli, C., & Chakraborty, S. (2024). How does the diurnal biological clock influence electrokinetics in a living plant? *Physics of Fluids*, 36(5), 52015.
- Heaney, M. B. (2004). Electrical conductivity and resistivity. In *In book: electrical measurement, signal processing, and displays, chapter:* 7 (pp. 1–14). CRC Press.
- Hellkvist, J., Richards, G. P., & Jarvis, P. G. (1974). Vertical gradients of water potential and tissue water relations in Sitka spruce trees measured with the pressure chamber. *Journal of Applied Ecology*, 11(2), 637–667.
- Hu, K., Loiseau, B., Carrière, S. D., & Jougnot, D. (2025). Self-potential signals related to tree transpiration in a Mediterranean climate. *Hydrology and Earth System Sciences*, 29(13), 2997–3018.
- Islam, M. M., Nagata, T., Nakao, S., & Miyazato, Y. (2024). Theoretical study of slightly underexpanded jets from elliptical nozzles\*. *Transactions of the Japan Society for Aeronautical and Space Sciences*, 67(1), 32–39.
- Ismayeel, M., Mehta, S. K., & Mondal, P. K. (2024). Maximizing blue energy via densely grafted soft layers in nanopores. *Langmuir*, 40(48), 25495–25508.
- Jafari, S., Khatibi, M., & Ashrafizadeh, S. N. (2024). Blue energy conversion utilizing smart ionic nanotransistors. *Electrochimica Acta*, 507, 145186.
- Jansen, S., Baas, P., Gasson, P., & Smets, E. (2003). Vestured pits: Do they promote safer water transport? *International Journal of Plant Sciences*, 164(3), 405–413. Published by: The University, 164(3), 405-413.
- Jensen, K. H., Berg-Sorensen, K., Bruus, H., & Bohr, T. (2016). Sap flow and sugar transport in plants. Reviews of Modern Physics, 88(3), 35007.
- Kaimoyo, E., Farag, M. A., Sumner, L. W., Wasmann, C., Cuello, J. L., & VanEtten, H. (2008). Sub-lethal levels of electric current elicit the biosynthesis of plant secondary metabolites. *Biotechnology Progress*, 24(2), 377–384.
- Karam, G. N. (2005). Biomechanical model of the xylem vessels in vascular plants. Annals of Botany, 95(7), 1179–1186.
- Khan, S. A., Dastagir, G., Uza, N. U., Muhammad, A., & Ullah, R. (2020). Micromorphology, pharmacognosy, and bio-elemental analysis of an important medicinal herb: *Verbascum thapsus* L. *Microscopy Research and Technique*, 83(6), 636–646.
- Khatibi, M., Ashrafizadeh, S. N., & Sadeghi, A. (2021). Augmentation of the reverse electrodialysis power generation in soft nanochannels via tailoring the soft layer properties. *Electrochimica Acta*, 395, 139221.
- Khatibi, M., Sadeghi, A., & Ashrafizadeh, S. N. (2021). Tripling the reverse electrodialysis power generation in conical nanochannels utilizing soft surfaces. *Physical Chemistry Chemical Physics*, 23(3), 2211–2221.
- Kielland. (1937). Ionic radii and diameters from several sources ionic diameters (pm) ionic radii in crystals (pm). Journal of the American Chemical Society, 59, 1675–1678.

- Krejčí, J., & Stoklasa, J. (2018). Aggregation in the analytic hierarchy process: Why weighted geometric mean should be used instead of weighted arithmetic mean. Expert Systems with Applications, 114, 97-106.
- Lee, S., & Oh, M. M. (2021). Electric stimulation promotes growth, mineral uptake, and antioxidant accumulation in kale (Brassica oleracea var. acephala). Bioelectrochemistry, 138, 107727.
- Lemström, S. (1904). Electricity in agriculture and horticulture, "The Electrician". Printing & Publishing Company, Limited.
- Li, S., Lens, F., Espino, S., & Jansen, S. (2016). Intervessel pit membrane thickness as a key determinant of embolism resistance in angiosperm xylem. IAWA Journal, 37(2), 152–171.
- Louf, J. F., Zheng, Y., Kumar, A., & Jensen, K. H. (2018). Imbibition in plant seeds. *Physical Review E*, 98(4), 1–5.
- Manhães, J. H. C., da Silva, D. C., Goncalves, Â.O., & Gomes, F. P. (2022). Effect of domestication on water transport in jatropha curcas seedlings: Relevance of xylem vessels of organs and aquaporin activity in roots. South African Journal of Botany, 150, 1069-1079.
- Mason, S. G. (1950). The electrokinetic properties of cellulose fibers. *Tappi*, 33(8), 413–417.
- Mehta, S. K., & Mondal, P. K. (2024). Electroosmotic mixing of viscoplastic fluids in a microchannel. *Physical Review Fluids*, 9(2), 23301.
- Melcher, P. J., Holbrook, N. M., Burns, M. J., & Sack, L. (2012). Measurements of stem xylem hydraulic conductivity in the laboratory and field. Methods in Ecology and Evolution, 3(4), 685–694.
- Millington, R. J., & Quirk, J. P. (1961). Permeability of porous solids. Transactions of the Faraday Society, 57, 1200–1207.
- Nikara, S., Ahmadi, E., & Nia, A. A. (2020). Effects of different preparation techniques on the microstructural features of biological materials for scanning electron microscopy. Journal of Agriculture and Food Research, 2, 100036.
- Panja, S., Mehta, S. K., Kalita, J., Prasad, M. K., & Mondal, P. K. (2024). Soft plant root structure-media flow interactions: Exploring the adverse effect of lead contamination in North-Eastern Indian rice. Physics of Fluids, 36(11), 111914.
- Park, K., Tixier, A., Paludan, M., Østergaard, E., Zwieniecki, M., & Jensen, K. H. (2021). Fluid-structure interactions enable passive flow control in real and biomimetic plants. Physical Review Fluids, 6(12), 123102.
- Paul, S., Choi, K. S., Lee, D. J., Sudhagar, P., & Kang, Y. S. (2012). Factors affecting the performance of supercapacitors assembled with polypyrrole/multi-walled carbon nanotube composite electrodes. Electrochimica Acta, 78, 649–655.
- Pivonka, P., & Smith, D. (2005). Investigation of nanoscale electrohydrodynamic transport phenomena in charged porous materials. International Journal for Numerical Methods in Engineering, 63(14), 1975–1990.
- Qaderi, M. M., Martel, A. B., & Dixon, S. L. (2019). Environmental factors influence plant vascular system and water regulation. Plants, 8(3), 65.
- Quintana-Pulido, C., Villalobos-González, L., Muñoz, M., Franck, N., & Pastenes, C. (2018). Xylem structure and function in three grapevine varieties. Chilean Journal of Agricultural Research, 78(3), 419–428.
- Roth, A. (1996). Water transport in xylem conduits with ring thickenings. Plant, Cell & Environment, 19(5), 622–629.
- Sadeghi, A., Azari, M., & Hardt, S. (2019). Electroosmotic flow in soft microchannels at high grafting densities. Physical Review Fluids, 4(6), 063701.
- Sarkar, S. (2020). Streaming-potential-mediated pressure-driven transport of Phan-Thien-Tanner fluids in a microchannel. Physical Review E, 101(5), 1-23.
- Schreiber, S. G., Hacke, U. G., & Hamann, A. (2015). Variation of xylem vessel diameters across a climate gradient: Insight from a reciprocal transplant experiment with a widespread boreal tree. Functional Ecology, 29(11), 1392–1401.
- Schulz, R., Ray, N., Zech, S., Rupp, A., & Knabner, P. (2019). Beyond Kozeny-Carman: Predicting the permeability in porous media. Transport in Porous Media, 130(2), 487-512.
- Scopa, A., Colacino, C., Lumaga, M. R. B., Pariti, L., & Martelli, G. (2009). Effects of a weak DC electric field on root growth in Arundo donax (Poaceae). Acta Agriculturae Scandinavica Section B: Soil and Plant Science, 59(5), 481–484.
- Sperling, O., Perry, A., Ben-Gal, A., Yermiyahu, U., & Hochberg, U. (2024). Potassium deficiency reduces grapevine transpiration through decreased leaf area and stomatal conductance. Plant Physiology and Biochemistry, 208, 108534.
- Teng, H. C., Kok, B. C., Uttraphan, C., & Yee, M. H. (2018). A review on energy harvesting potential from living plants: Future energy resource. International Journal of Renewable Energy Research, 8(4), 2398–2414.
- Teodoro, C., Arcos, J., Bautista, O., & Méndez, F. (2024). Electro-poroelastohydrodynamics of the endothelial glycocalyx layer and streaming potential in wavy-wall microvessels. Physical Review Fluids, 9(1), 013101.
- Thi, T., Thu, P., Yasui, H., & Yamakawa, T. (2017). Soil science and plant nutrition effects of salt stress on plant growth characteristics and mineral content in diverse rice genotypes. Soil Science and Plant Nutrition, 63(3), 264–273.
- van Doorn, W. G., Hiemstra, T., & Fanourakis, D. (2011). Hydrogel regulation of xylem water flow: An alternative hypothesisspi. Plant Physiology, 157(4), 1642–1649.
- Vanýsek, P. (1972). Ionic conductivity and diffusion at infinite dilution handbook of electrolyte solutions. Physical Science Data Series, 2, 2–226.
- Vasu, N., & De, S. (2010). Electroviscous effects in purely pressure driven flow and stationary plane analysis in electroosmotic flow of power-law fluids in a slit microchannel. International Journal of Engineering Science, 48(11), 1641–1658.
- Venkata Mohan, S., & Yeruva, D. K. (2023). In situ self-induced electrical stimulation to plants: Modulates morphogenesis, photosynthesis and gene expression in Vigna radiata and Cicer arietinum. Bioelectrochemistry, 154, 108550.
- Wang, Y. Q., & Wang, J. H. (2004). Effect of electric fertilizer on soil properties. Chinese Geographical Science, 14(1), 71–74.
- Wen, L., Wang, X., Xu, Q., & Xia, C. (2023). Impacting factors of changes in dynamic viscosity and interfacial tension of wood xylem sap. Forests, 14(7), 1344.

- Xie, Z., Chen, X., & Tan, F. (2024). Electrokinetic flow and energy conversion induced by streaming potential in nanochannels with symmetric corrugated walls. *Physics of Fluids*, 36(9), 092016.
- Xu, T., Zhang, L., & Li, Z. (2020). Computational fluid dynamics model and flow resistance characteristics of *Jatropha curcas* L. xylem vessel. *Scientific Reports*, 10(1), 14728.
- Xu, T., Zhi, S., Su, Y., Li, Z., & Zheng, E. (2022). Water transport characteristics of multiple structures of xylem vessels in magnolia. Forests, 13(10), 1617.
- Xu, T., Zhi, S., Zheng, E., & Yan, C. (2021). Flow resistance characteristics of the stem and root from conifer (*Sabina chinensis*) xylem tracheid. *PLoS One*, 16, 1–16.
- Yugang, Z., & Hongyi, D. (2013). Xylem vessel element structure explains why columnar apple trees flower early and have higher yield, African Journal of Agricultural Research, 8(31), 4194–4197.
- Zimmermann, R., McDonald, K., Oren, R., & Way, J. (1995). Xylem dielectric constant, water status, and transpiration of young Jack Pine (*Pinus banksiana* Lamb.) in the southern boreal zone of Canada. In: 1995 International Geoscience and Remote Sensing Symposium, IGARSS '95. Quantitative Remote Sensing for Science and Applications (Vol. 2, pp. 1006–1008).

Cite this article: Kalita J., Mehta S. and Mondal P. (2025). Unveiling mysteries of micro-porous structures in xylem vascular of plants: characterising nutrient transport using electro-hydrodynamics. *Flow*, 5, E38. https://doi.org/10.1017/flo.2025.10031